

## CHAPTER - 4

### Results and Discussion

This chapter presents a detailed characterization of five phases. Results from Phase I and Phase III are shown with the addition of modifiers, whereas Phases II, IV, and V include no modifiers. The fixed 2.5 wt.% of high-temperature oxides are added to the Al 7075 alloy. The separate addition of oxides like  $ZrO_2$ ,  $TiO_2$ , and  $ZrTiO_4$  acts as a modifier in the melt. The effect of variation of quenching media, and different casting techniques, is also included in Phase II, and Phase IV, respectively. Finally, Phase V includes the preparation of cost-effective cast Al 7075 by using available scrap, and by alloying controlling sequences.

#### 4.1 Investigation of raw materials

The received materials were checked for chemical analysis by optical emission spectroscopy. The Thermo Fisher Scientific model ARL™ iSpark 8860 Fire Assay machine was used to perform chemical analysis. A bulk chemical analysis of the as-received Al-7075 is presented in Table 4.1.

**Table 4.1 Spectroscopy analysis of as-received Al 7075.**

Element (wt. %)	Zn	Mg	Cu	Mn	Al
Average	5.48	2.25	1.54	0.09	90.64

The composition of Al 7075 is within the limit, as per the aluminium association. Table 4.2 represents the physical and chemical properties of high-temperature oxides. The chemical analysis is done using energy-dispersive spectroscopy. The particle size determination is performed using SEM (JEOL 5610LV). The SEM images of the investigation are displayed in Figure 4.1 (a) to (f). An average particle size is measured for each powder sample. The non-agglomerated powder particle size ranges between 2 to 6 microns.

Table 4.2 Physical properties and Chemical analysis of high-temperature oxides.

High-temperature oxides (Powder Form)	Density (g/cc) (ref. [285, 286])	Crystal Structure	Chemical Analysis by SEM/EDS (wt. %)			Particle Size Measurement by SEM
			Zr	Ti	O	
Zirconium Oxide (ZrO <sub>2</sub> )	5.68	Monoclinic	64.61	--	35.39	2-6 microns
Titanium Oxide (TiO <sub>2</sub> )*	4.23	Tetragonal	--	29.80	57.36	
Zirconium Titanate (ZrTiO <sub>4</sub> )	4.82	Orthorhombic	25.20	25.10	49.70	

\*impurities such as Ca & Si in 3.42 & 9.24 wt. % respectively.

The ZrO<sub>2</sub> and ZrTiO<sub>4</sub> powders are pure, but the TiO<sub>2</sub> powder has an impurity content of 3.5 and 9.0 wt.% Ca and Si, respectively.

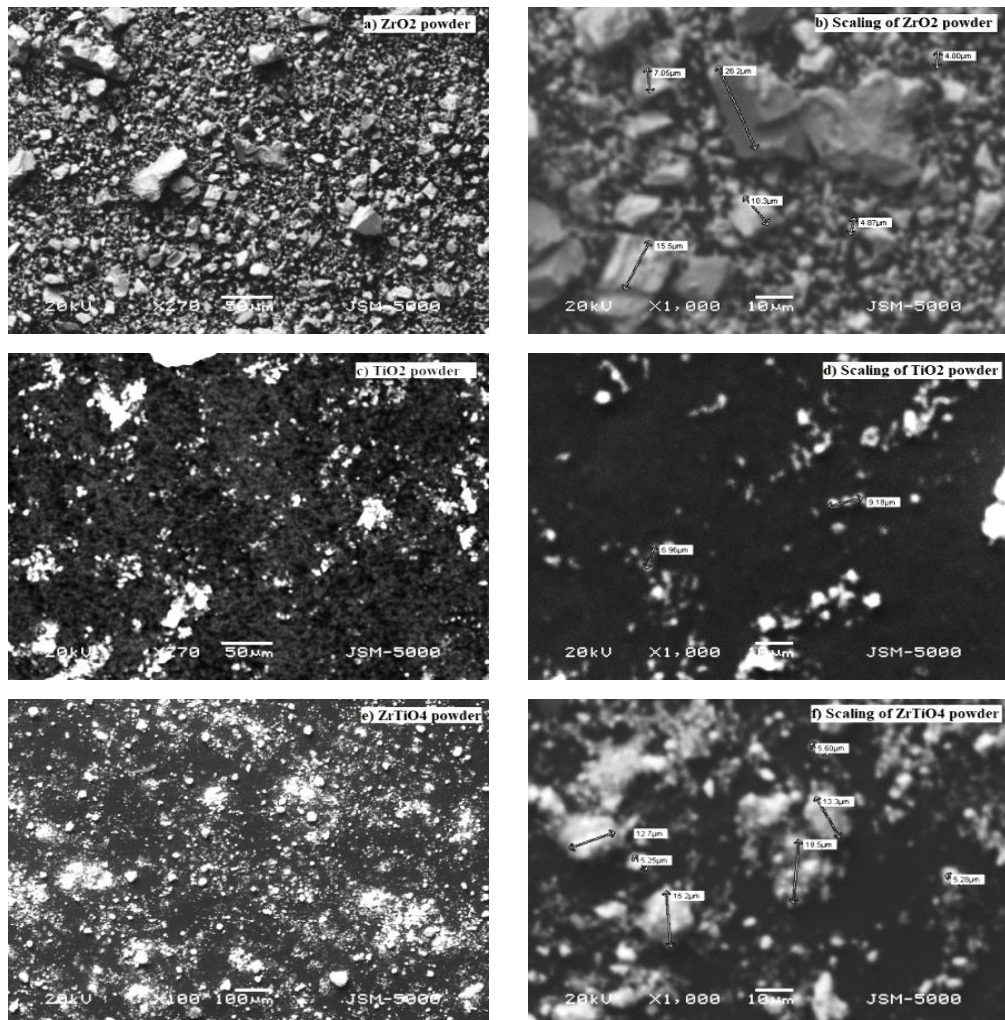


Figure 4.1 SEM images and particle size measurement of oxide powder a) ZrO<sub>2</sub> Powder; b) scaling of ZrO<sub>2</sub> powder; c) TiO<sub>2</sub> powder; d) scaling of TiO<sub>2</sub> powder; e) ZrTiO<sub>4</sub> powder; f) scaling of ZrTiO<sub>4</sub>.

## 4.2 Phase I: Effect of the oxide addition into cast Al 7075

The high-temperature oxides like  $ZrO_2$ ,  $TiO_2$ , and  $ZrTiO_4$  are added separately to the Al 7075 with a fixed 2.5 weight percentage. The four systems are formed:

**System A** → As-cast Al 7075.

**System B** → cast Al 7075+2.5 wt.%  $ZrO_2$ .

**System C** → Cast Al 7075+2.5 wt.%  $TiO_2$ .

**System D** → Cast Al 7075+2.5 wt.  $ZrTiO_4$ .

### 4.2.1 Chemical analysis of oxide-added Al 7075

After the addition of the oxide in Al 7075, the bulk chemical composition of Al 7075 is presented in Table 4.3.

**Table 4.3** Mass spectroscopy analysis of Al 7075 after casting; a) as-cast, b) 2.5 wt.% added  $ZrO_2$ , c) 2.5 wt.% added  $TiO_2$ , d) 2.5 wt.% added  $ZrTiO_4$ .

Systems	Elements (wt.%)					
	Zn	Mg	Cu	Cr	Zr	Ti
A	5.7223	2.4270	1.8060	0.2050	0.0001	0.0003
B	5.9810	2.2360	1.6180	0.2120	0.0118	0.0040
C	5.8821	2.2290	1.5490	0.2040	0.0103	0.0280
D	6.0630	2.2870	1.6780	0.2050	0.0115	0.0290

Mass spectroscopy verified Zr and Ti at the macroscopic level. The EDS analysis revealed Zr and Ti at the local microscopic level, which is shown in Table 4.4. The JOEL JSM-5610LV is used to perform EDS analysis.

**Table 4.4** Recovery of Zr, and Ti by EDS analysis of the developed system of Al 7075 after casting.

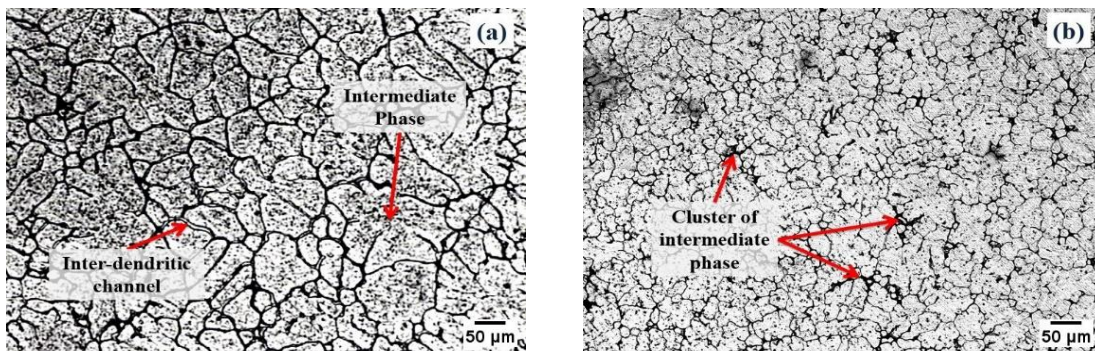
Alloy System	Wt.% Zr	Wt.% Ti
A	---	---
B	0.04 – 0.22	---
C	---	0.01 – 0.05
D	0.36 – 0.77	0.03 – 0.04

## 4.2.2 Microscopy of Phase I

### 4.2.2.1 Optical microscopy

Many aluminium alloys are noted to solidify in dendritic patterns. These patterns are usually the consequence of broad solidification temperature ranges where major components are solidified first, in a dendritic or tree-like form, while the remaining fluid in the material fills in the gaps between dendrites. The metal cracking is caused by inadequate backfill, internal shrinking stresses, and weak grain boundaries. Solidification causes hot tearing. Hot tearing renders the material unusable for structural roles. Inoculants act as heterogeneous nucleation sites to stop hot tearing in aluminium alloys. The second phase particles form heterogeneous nucleation sites. Fine grain structure is promoted by well-dispersed nucleation sites [287].

The optical micrographs are examined to study the morphology of as-cast and oxide-added Al 7075. The microstructure of as-cast 7075 aluminium alloy is shown in Figure 4.2 (a). It shows a combination of equiaxed and columnar crystals of the  $\alpha$ -Al matrix. The intermediate phases are within an inter-dendritic channel. The black colour phase is a non-equilibrium eutectic structure located randomly between cellular cells, and it has been reported by many researchers [163, 205, 288]. It denotes the primary  $\alpha$ (Al) phase, which is concluded by black boundaries of intermetallic phases. The intermetallic phases,  $\eta$ (MgZn<sub>2</sub>), T(Al<sub>2</sub>Mg<sub>3</sub>Zn<sub>3</sub>), S(Al<sub>2</sub>CuMg), and  $\theta$ (Al<sub>2</sub>Cu) are the most typically found in the as-cast microstructure of the 7XXX series aluminium alloys [289, 290]. Some intermetallic phases are also present at the centre of the grains. The white portion denotes the  $\alpha$ (Al) phase, while the black portions denote the intermetallic phase [25]. The tensile property of as-cast 7075 Al alloy is reduced by a continuous network of thick eutectic phases as intermetallic such as  $\eta$ (MgZn<sub>2</sub>), T(Al<sub>2</sub>Mg<sub>3</sub>Zn<sub>3</sub>), and S(Al<sub>2</sub>CuMg) [291]. The presence of dispersoid particles leads to a change in the recrystallization behaviour of the alloy [292–295]. Hence, the addition of oxide can change distribution patterns of the eutectic phase, as shown in Figure 4.2 (b), 4(c), and 4(d).



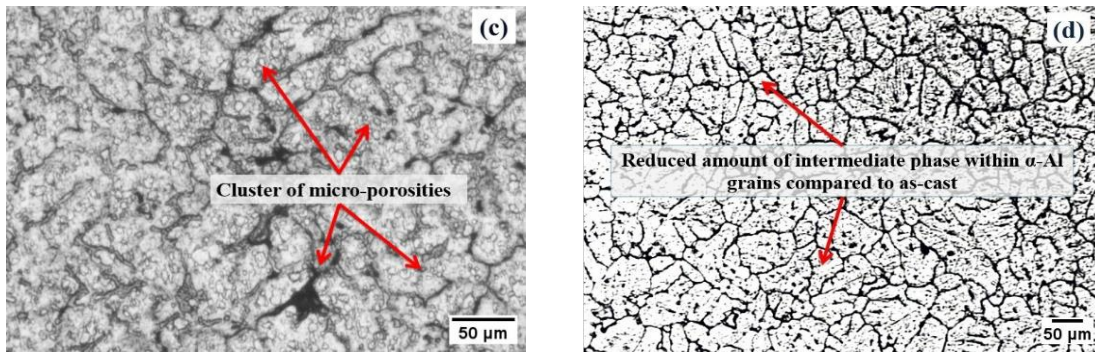


**Figure 4.2** Optical microstructure of Al7075; (a) as-cast; and 2.5 wt.% added (b) ZrO<sub>2</sub>; (c) TiO<sub>2</sub>; (d) ZrTiO<sub>4</sub>.

Figure 4.2 (b) shows the microstructure of ZrO<sub>2</sub> oxide addition in the Al 7075. The difference in the formation of grain morphology differs from the as-cast microstructure. During the solidification process, Zr and Al atoms form massive fine Al<sub>3</sub>Zr particles that are coherent into the  $\alpha$ -Al matrix. Because of the coherency in the crystal lattice, the XRD peak may be near to aluminium lattice. In addition, the amount of Al<sub>3</sub>Zr phase might be less than 2 wt.%, so it may not be recognised by XRD analysis. However, the localized presence of zirconium was confirmed by SEM-EDS analysis. ZrO<sub>2</sub> addition in the melt acts as a heterogeneous nucleation site for the formation of  $\alpha$ -Al nuclei. Compared to the as-cast, the grains are transformed from columnar to equiaxed, and cellular dendrites to columnar dendrites [205]. Finally, significant refinement of the  $\alpha$ -Al matrix and dendritic morphology was observed. The refinement observed because of the heterogeneous nucleation site creates a low ( $G_L/R$ ) ratio and favours the equiaxed grain morphology rather than columnar anisotropic grains.

The TiO<sub>2</sub>-added microstructure is observed in Figure 4.2 (c). It shows the clustered micro-porosities that weaken the strength. Along with micro-porosities, because of the globular growth of the  $\alpha$ -Al matrix and intermediate phase distribution, substantial improvement in hardness and tensile strength were observed compared to the as-cast sample. As reported by Xinwei Li et al. [206], the excess amount of TiN particles aggregates together and reduces the chances of a heterogeneous nucleation site; a similar phenomenon is possible with the TiO<sub>2</sub> particle. Finally, the grain size of TiO<sub>2</sub>-added alloy becomes larger. The ZrTiO<sub>4</sub>-added microstructure is presented in Figure 4.2 (d). It is like the as-cast. The columnar dendrite with a reduced amount of intermediate phase is observed. The inter-dendritic channels are narrowed down compared to the as-cast, but the mechanical properties are more or less similar. When the presence of Zr and Ti together as oxides, there is significantly less chance

of forming the primary nucleating site of the  $\text{Al}_3\text{Zr}/\text{Al}_3(\text{Zr, Ti})$  phase, and ultimately does not alter the microstructure significantly [167].

4.2.2.2 Localised SEM-EDS analysis and intermediate phases

The presence of Ti and Zr after adding 2.5 wt. % of oxide, it is necessary to carry out SEM-EDS testing. The overall presence of Zr and Ti is significantly less. However, the localized presence can be confirmed by the SEM-EDS. The point EDS and area EDS were taken for all samples to study the intermediated phase distribution, as shown in Figure 4.3 (a) to (h).

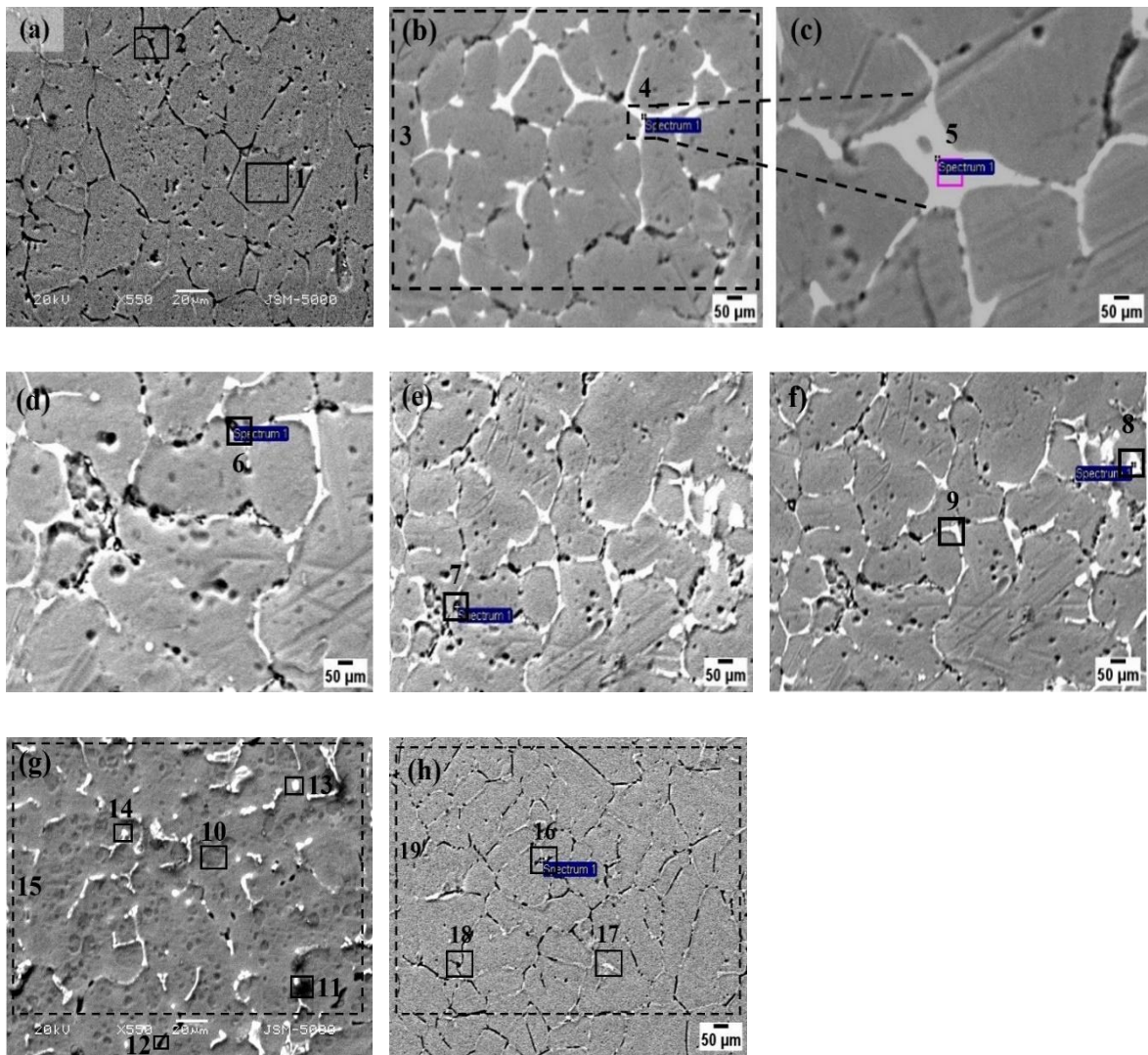


Figure 4.3 SEM photographs of (a) as-cast Al7075; (b to f)  $\text{ZrO}_2$ -added Al7075; (g)  $\text{TiO}_2$ -added Al7075; (h)  $\text{ZrTiO}_4$  added Al7075.

**Table 4.5 EDS analysis of the selected point/area in Figure 4.3. (in wt.%) and closest phases.**

System	Points	Al	Zn	Mg	Cu	Zn/Mg	Closest Phase
As-cast	1	100.00	0.00	0.00	0.00	0.00	$\alpha$ (Al)
	2	99.65	0.11	0.24	0.00	0.46	T( $\text{Al}_2\text{Mg}_3\text{Zn}_3$ )
ZrO <sub>2</sub> added	3 (Zr 0.05)	90.26	5.94	1.96	1.80	3.03	$\eta$ (MgZn <sub>2</sub> )
	4 Zr (0.19)	50.53	23.07	11.18	15.04	2.06	T( $\text{Al}_2\text{Mg}_3\text{Zn}_3$ )
	5 (Zr 0.22)	45.84	24.77	12.66	16.55	1.96	T( $\text{Al}_2\text{Mg}_3\text{Zn}_3$ )
	6 (Zr 0.07)	69.42	12.44	3.07	13.88	4.06	$\eta$ (MgZn <sub>2</sub> )
	7 (Zr 0.04)	79.11	7.75	2.74	2.51	2.83	$\eta$ (MgZn <sub>2</sub> )
	8	87.14	4.85	2.36	1.42	2.06	$\eta$ (MgZn <sub>2</sub> )
	9	41.88	17.27	10.37	13.4	1.67	T( $\text{Al}_2\text{Mg}_3\text{Zn}_3$ )
	10 (Ti 0.10)	91.38	3.88	1.05	0.45	3.70	$\eta$ (MgZn <sub>2</sub> )
	11	42.29	2.84	2.04	0.56	1.39	T( $\text{Al}_2\text{Mg}_3\text{Zn}_3$ )
TiO <sub>2</sub> added	12 (Ti 0.01)	65.59	5.97	9.70	1.84	0.62	T( $\text{Al}_2\text{Mg}_3\text{Zn}_3$ )
	13	66.60	12.03	3.51	8.21	3.43	$\eta$ (MgZn <sub>2</sub> )
	14	55.77	2.01	0.90	2.39	2.23	$\eta$ (MgZn <sub>2</sub> )
	15 (Ti 0.05)	84.90	4.99	1.56	1.28	3.20	$\eta$ (MgZn <sub>2</sub> )
ZrTiO <sub>4</sub> added	16 (Zr 0.36)	80.75	0.03	1.07	0.00	0.03	$\alpha$ (Al)
	17 (Ti 0.03)	81.46	0.00	0.39	0.00	0.00	$\alpha$ (Al)
	18 (Zr 0.77)	91.96	0.00	0.99	0.00	0.00	$\alpha$ (Al)
	19 (Ti 0.04)	95.87	0.00	0.47	0.00	0.00	$\alpha$ (Al)

Table 4.5 shows the EDS analysis of all samples. Points 1 and 2 are the EDS results of the as-cast sample presented in Figure 4.3 (a). It shows the  $\alpha$ -Al phases during the solidification. The SEM images of Figure 4.3 (b to f) show the white intermediate phases at the grain boundaries of the  $\alpha$ -Al matrix. The white intermediate phase proportion is higher in the ZrO<sub>2</sub> and TiO<sub>2</sub>-added samples compared to ZrTiO<sub>4</sub> and as-cast samples. In the last decade, many researchers reported intermediate phases of Al-Zn-Mg-Cu, such as MgZn<sub>2</sub>, Al<sub>2</sub>CuMg, Al<sub>2</sub>Mg<sub>3</sub>Zn<sub>3</sub>, and Al<sub>7</sub>Cu<sub>2</sub>Fe. Zn, Mg, and Cu content determined the formation of these phases. Zn and Mg content significantly play a vital role in forming ( $\eta$ ) MgZn<sub>2</sub> and (T) Al<sub>2</sub>Mg<sub>3</sub>Zn<sub>3</sub> phases based on the Zn/Mg ratio. When the Zn/Mg ratio > 2 forms the  $\eta$  phase, the T phase forms when the Zn/Mg ratio < 2. Therefore, higher Mg content increases the probability of forming the T phase [296, 297]. The higher Cu content forms the  $\eta$  phase instead of forming the S phase. The amount of the T phase increases when Cu content increases with a decreasing Zn/Mg ratio [165]. Points 3 to 9 are EDS analyses of the ZrO<sub>2</sub>-added sample. The

( $\eta$ )  $\text{MgZn}_2$  and (T)  $\text{Al}_2\text{Mg}_3\text{Zn}_3$  are the closest phases at different points based on the Zn/Mg ratio. Similarly, points 10 to 15 are EDS analyses of the  $\text{TiO}_2$ -added sample, and points 16 to 19 are of the  $\text{ZrTiO}_4$ -added sample, as shown in Figure 4.3 (g) and Figure 4.3 (h), respectively. The ( $\eta$ )  $\text{MgZn}_2$  and (T)  $\text{Al}_2\text{Mg}_3\text{Zn}_3$  are the closest phases in the  $\text{TiO}_2$ -added sample, while it is absent from the  $\text{ZrTiO}_4$ -added sample. In the case of the  $\text{ZrTiO}_4$ -added sample, there is no recovery of Zr and Ti; hence, it has similar phases to the as-cast material.

#### 4.2.3 XRD analysis of as-cast and oxide added Al 7075

Figure 4.4 shows the XRD pattern comparison of systems A, B, C, and D. The XRD pattern of system A shows the confirmation of the significant  $\alpha(\text{Al})$  along with the intermediate phase of  $\text{Al}_{0.95}\text{Mg}_{0.05}$  (ref. card 98-009-8729), and  $\text{Al}_5\text{Cu}_6\text{Mg}_2$  (98-006-5716). System B confirms the phase of  $\text{Al}_{3.7}\text{Mg}_{0.3}$  (98-008-4528),  $\text{Al}_3\text{Zr}_1$  (98-008-4802), and  $\text{Mg}_1\text{Zn}_2$  (98-001-8378) along with significant  $\alpha(\text{Al})$ . The EDS analysis in Table 4.5 confirms the same phase. In system C, along with major  $\alpha\text{-Al}$ ,  $\text{Ti}_1$  (98-002-3322),  $\text{Al}_1\text{Ti}_1$  (98-008-0573), and  $\text{Mg}_1\text{Zn}_2$  (98-010-2888) phases confirm by XRD analysis. The same phases are already confirmed by EDS analysis and are presented in Table 4.5.

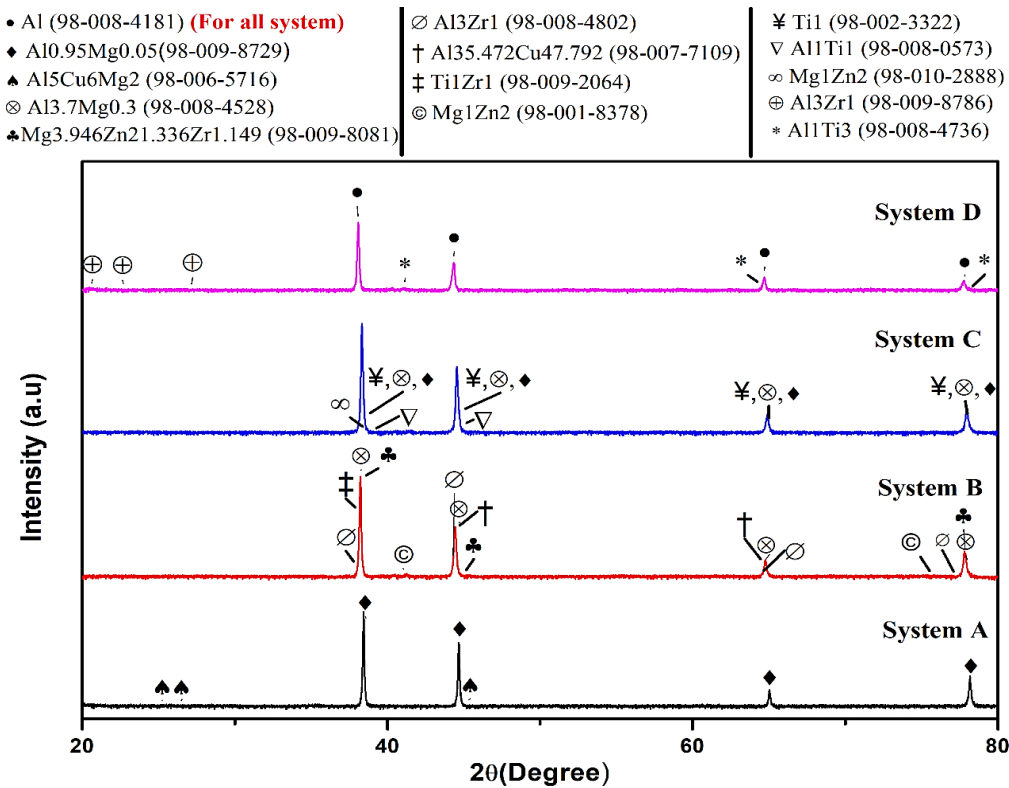


Figure 4.4 XRD patterns of Al7075 systems; A) as-cast; B)  $\text{ZrO}_2$ ; C)  $\text{TiO}_2$ ; and D)  $\text{ZrTiO}_4$ .

Similarly, in system D, the confirmation of phases is  $\text{Al}_3\text{Zr}_1$  (98-009-8786) and  $\text{Al}_1\text{Ti}_3$  (98-008-4736). The morphology of Ti-bearing dispersoids is close to the Al–Zr phase. Also, the crystalline lattice of  $\text{Al}_3\text{Zr}$  and  $\text{Al}_3\text{Ti}$  is identical. The combined effect of Al–Zr and Al–Ti phases on the microstructure and mechanical properties is negligible [95,298]. Therefore, there is no improvement in microstructure and mechanical properties observed in  $\text{ZrTiO}_4$ -added Al7075

#### 4.2.4 Grain size measurement

The histograms of grain size measurement and grain area measurement are shown in Figure 4.5 (a) to (d), and Figure 4.6 (a) to (d), respectively. The ImageJ software is used to get the set of data and plotted in the Origin.

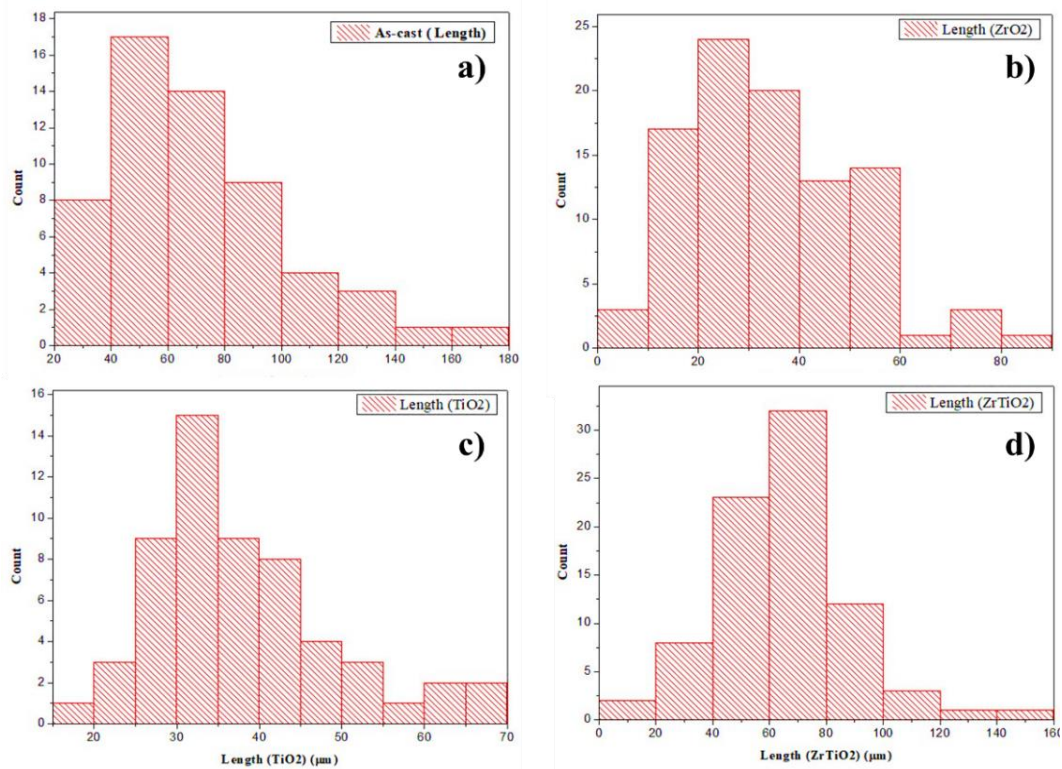
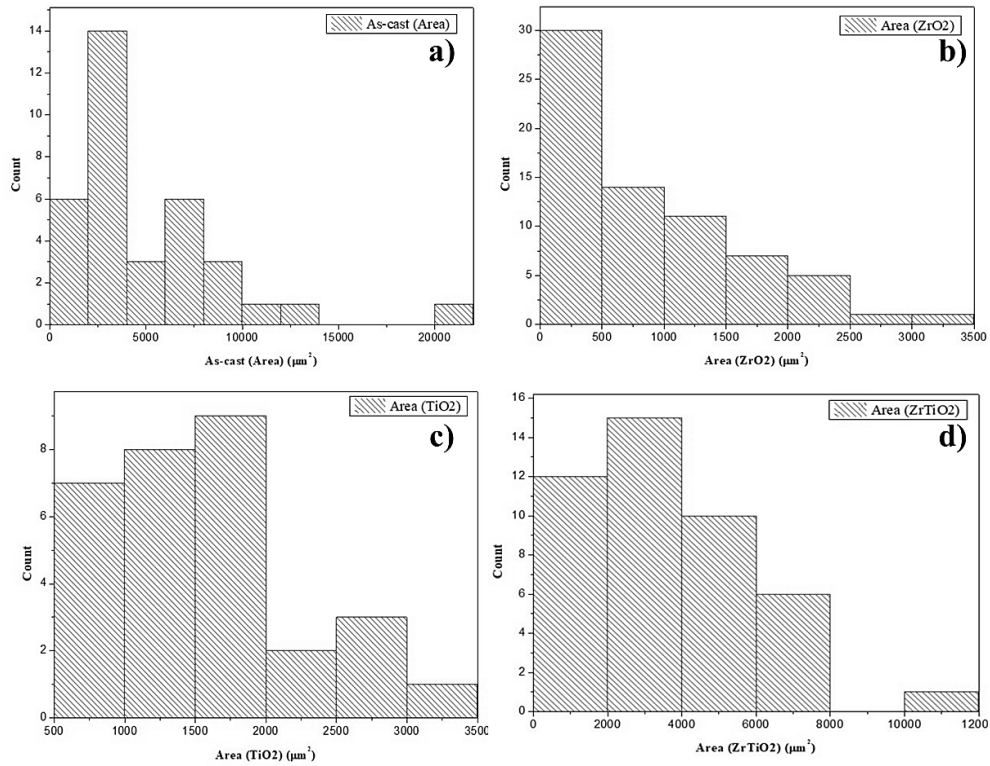


Figure 4.5 Grain size measurement of Al7075; (a) as-cast; and 2.5 wt.% added (b)  $\text{ZrO}_2$ ; (c)  $\text{TiO}_2$ ; (d)  $\text{ZrTiO}_4$ .



**Figure 4.6 Grain area measurement of Al7075; (a) as-cast; and 2.5 wt.% added (b) ZrO<sub>2</sub>; (c) TiO<sub>2</sub>; (d) ZrTiO<sub>4</sub>.**

The above histograms and Table 4.6 illustrate the grain size reduction, that is observed in Al 7075 with ZrO<sub>2</sub> and TiO<sub>2</sub> added, as compared to the as-cast, and ZrTiO<sub>4</sub> added Al 7075.

**Table 4.6 Min., max., and mean grain size and area of all the systems**

System	Grain Length (μm)			Grain Area (μm <sup>2</sup> )		
	Min.	Max.	Mean	Min	Max	Mean
As-cast	29.82	176.80	70.20	1257.74	21104.08	4987.71
ZrO <sub>2</sub> -added	9.16	82.63	34.53	92.97	3074.63	884.01
TiO <sub>2</sub> -added	19.69	68.52	37.86	623.06	3063.98	1559.44
ZrTiO <sub>4</sub> -added	17.64	148.5	65.27	721.84	11748.45	3635.74

#### 4.2.5 Mechanical properties

These samples are subjected to mechanical tests such as Brinell, micro-hardness, and tensile strength. The test results are presented in Figure 4.7. ZrO<sub>2</sub>-added samples show a hardness of 112 BHN, which is 52% higher than the as-cast 7075 Al alloy. Micro-hardness value also becomes 56% higher than as-cast 7075 Al alloy. The uniform distribution of the non-

equilibrium eutectic phase and the development of finer  $\alpha(\text{Al})$  grains because of the inhibition of recrystallization given by  $\text{Al}_3\text{Zr}$  dispersoids are the basis of the increase in hardness. The micro-hardness indentation depth decreased from 15.58  $\mu\text{m}$  to 11.74  $\mu\text{m}$ , as shown in Table 4.7. The hardness values of as-cast and 2.5 wt.%  $\text{ZrTiO}_4$  are relatively similar. It is because of the minimal interaction between Zr & Ti atoms when combined and finally does not alter the microstructure of the  $\text{ZrTiO}_4$  added sample [95]. Several researchers were working on oxide-added aluminium alloys. They found that with 2.5 wt.%  $\text{ZrO}_2$  added sample shows better mechanical properties at the cost of ductility.

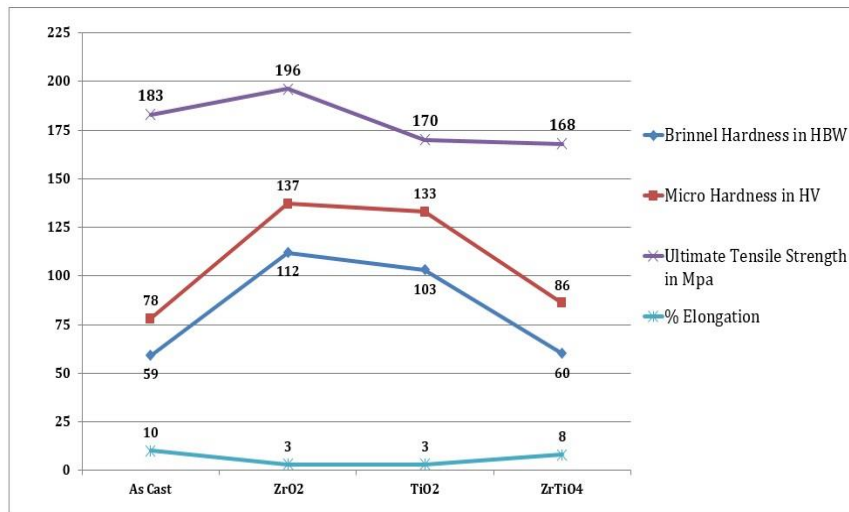


Figure 4.7 Graphical presentation of mechanical properties of Al 7075; as-cast, and 2.5 wt.% added oxides.

Table 4.7 Comparison of mechanical properties of cast Al7075 with oxide-added samples.

Mech. Properties	Alloy System			
	A	B	C	D
Hardness (BHN)	59	112	103	60
Micro-hardness (HV.)	78	137	133	86
Indentation depth ( $\mu\text{m}$ )*	15.58	11.74	11.91	14.82
Tensile Strength (MPa)	183	196	170	168
Elongation (%)	10%	3%	3%	8%

\*Indentation depth of micro-hardness.

#### 4.2.6 Structure-property relationship

Relative Hall-Petch relationship is established based on micro-hardness versus grain diameter, as shown in Figure 4.8. It is well known that the strength of the material increases as the grain size is reduced, according to the Hall-Petch equation. Li et al. [206] established a

correlation between hardness and grain size for as-cast Al-Zn-Mg-Cu and 0 to 0.5 wt.% TiN/Ti grain refiner, and found that primary  $\alpha$ -Al grains size drastically reduced from 400  $\mu\text{m}$  to 78.5  $\mu\text{m}$  [206]. The relative Hall-Petch equation is  $H_v = H_0 + kD^{-1/2}$ , where  $H_0$  and  $k$  are the constant.

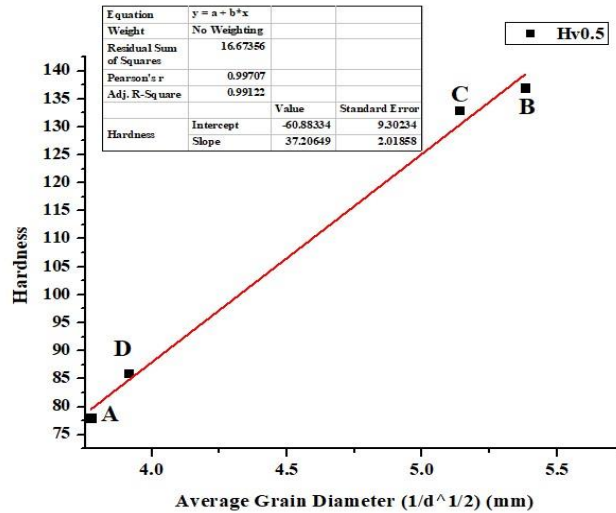


Figure 4.8 The plot of micro-hardness of as-cast, and oxide-added Al 7075 versus grain size ( $D^{-1/2}$ ).

Chokshi et al. [97] investigated the Hall-Petch relation using hardness value. So, the above graph satisfies the condition of grain size reduction improves the mechanical properties.

#### 4.2.7 Natural ageing behaviour of as-cast and oxide added Al 7075

The as-cast and oxide-added Al 7075 microstructural samples were put for 2 years of natural ageing. The morphology study, eutectic phase shifting, and hardness values are recorded for comparison.

##### 4.2.7.1 Microscopy of natural ageing of oxide added Al 7075 (Phase I)

Microstructural morphology changes with time, as shown in Figure 4.9 (a) to (d). The dissolution of intermediate phases is observed in as-cast, and  $\text{ZrTiO}_4$  added Al 7075, as shown in Figure 4.9 (a) and (d), respectively. While the grain boundary precipitation was observed in  $\text{ZrO}_2$ ,  $\text{TiO}_2$  added Al 7075, as shown in Figure 4.9 (b) and (c). Wen et al. [299] investigated the dissolution of the secondary phase at different solid solution temperatures, concentrating on the diffusion of atoms like Mg, Zn and Cu.

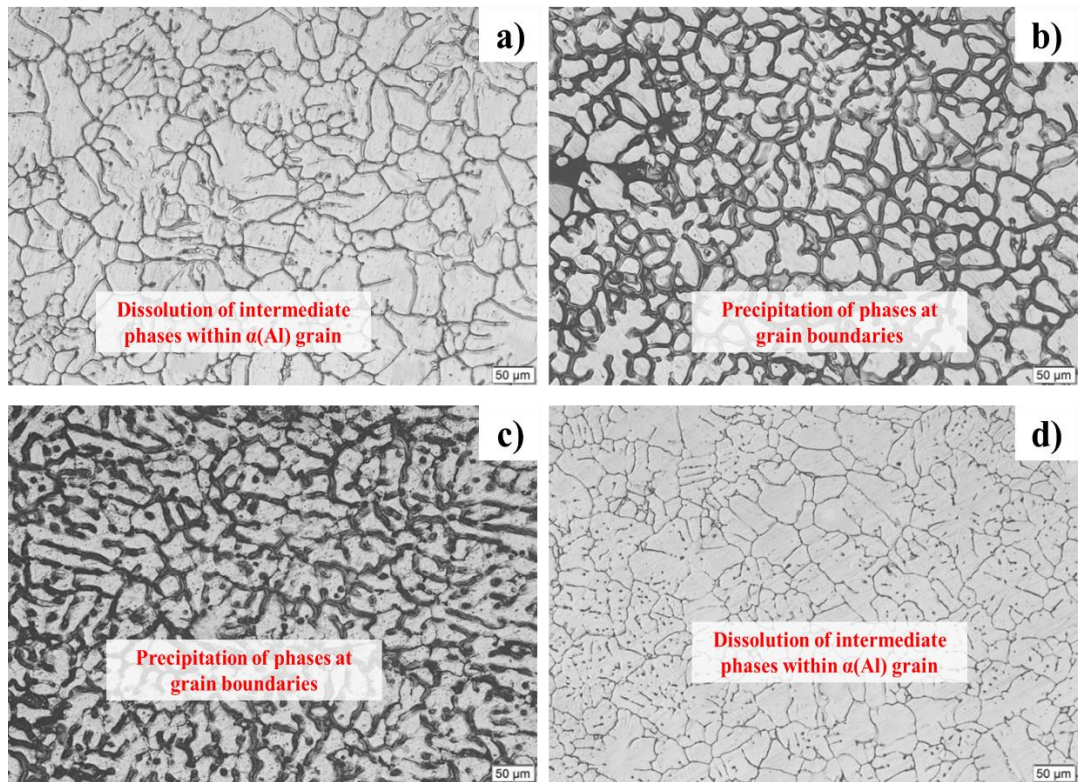


Figure 4.9 Micrograph of natural ageing of oxide added Al 7075 (a) as-cast, and 2.5 wt.% added (b)  $ZrO_2$ ; (c)  $TiO_2$ ; (d)  $ZrTiO_4$ .

4.2.7.2 Analytical SEM study

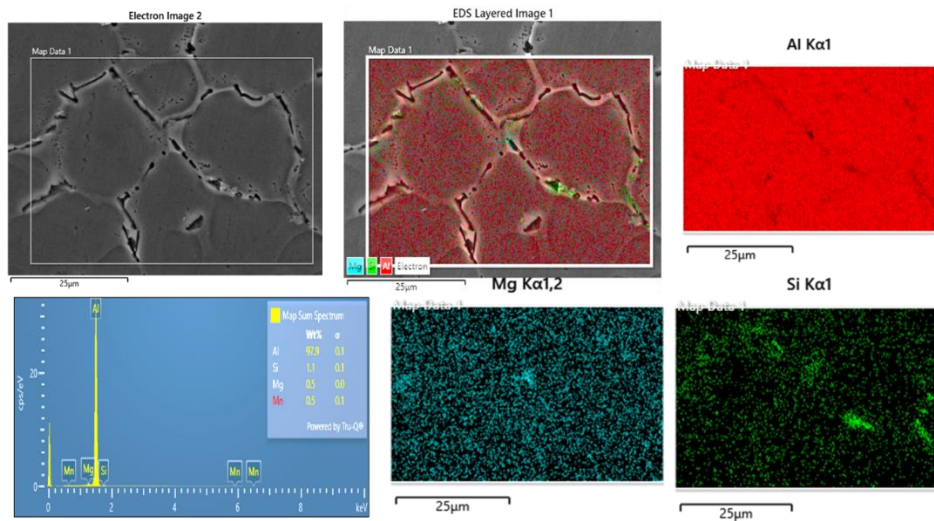


Figure 4.10 As-cast Al 7075 SEM-EDS area mapping.

Figure 4.10 shows the dissolution of the alloying element in the  $\alpha(Al)$  grain.

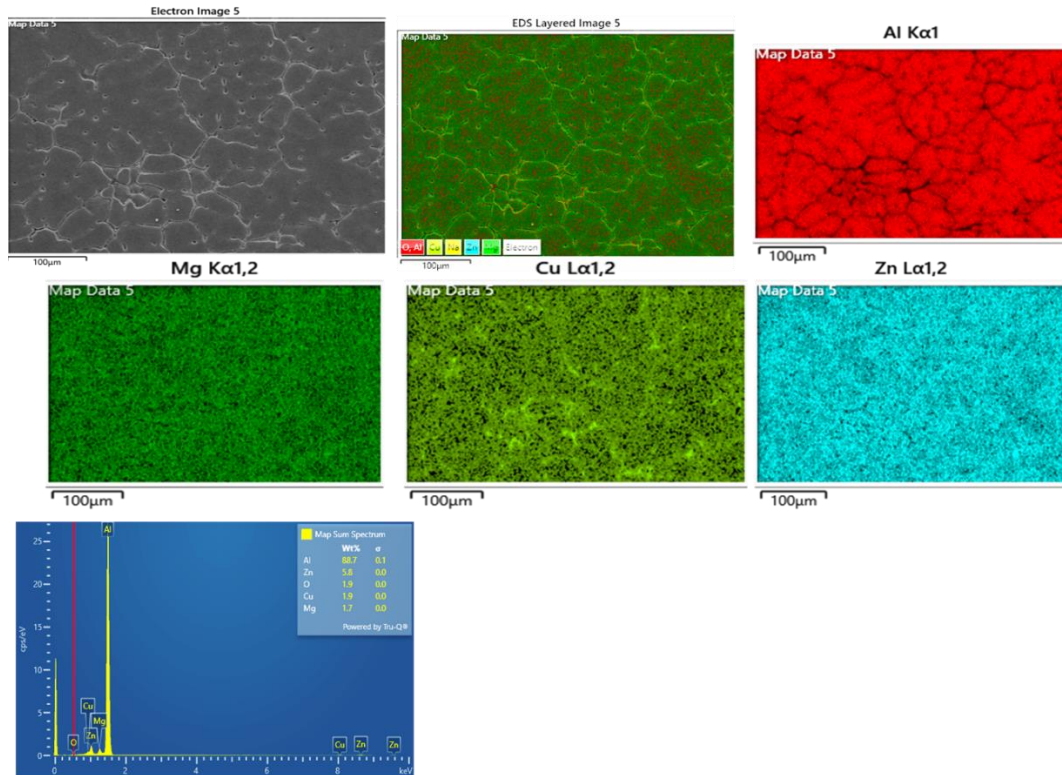


Figure 4.11 SEM-EDS area mapping of ZrO<sub>2</sub> added Al 7075.

The alloying element does not experience the same dissolution in Figure 4.11 as in as-cast Al 7075. Similarly, Figure 4.12, shows the dispersed distribution of zinc and magnesium, while a copper-rich grain boundary is observed around α(Al) grain.

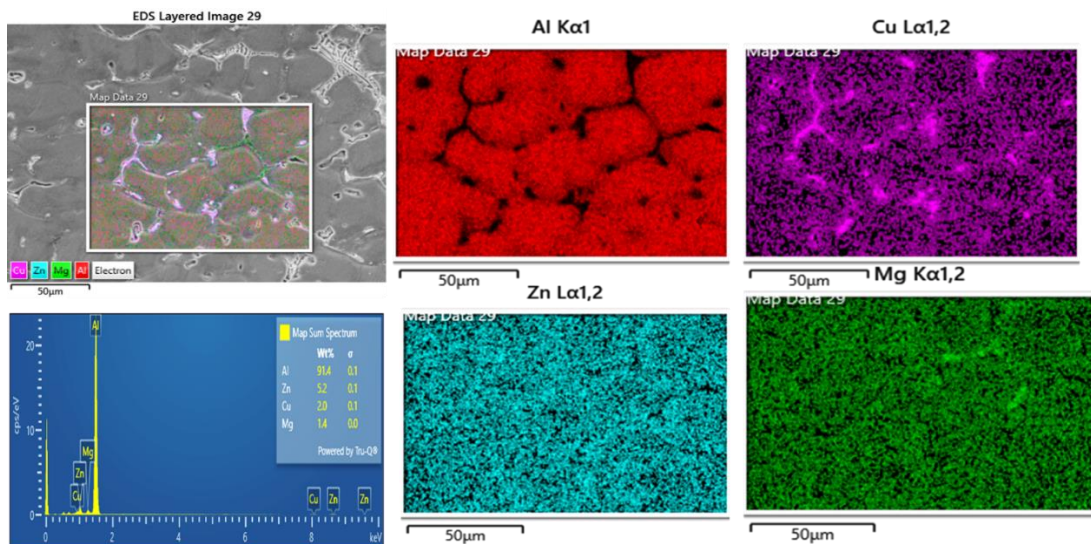


Figure 4.12 SEM-EDS area mapping of TiO<sub>2</sub> added Al 7075.

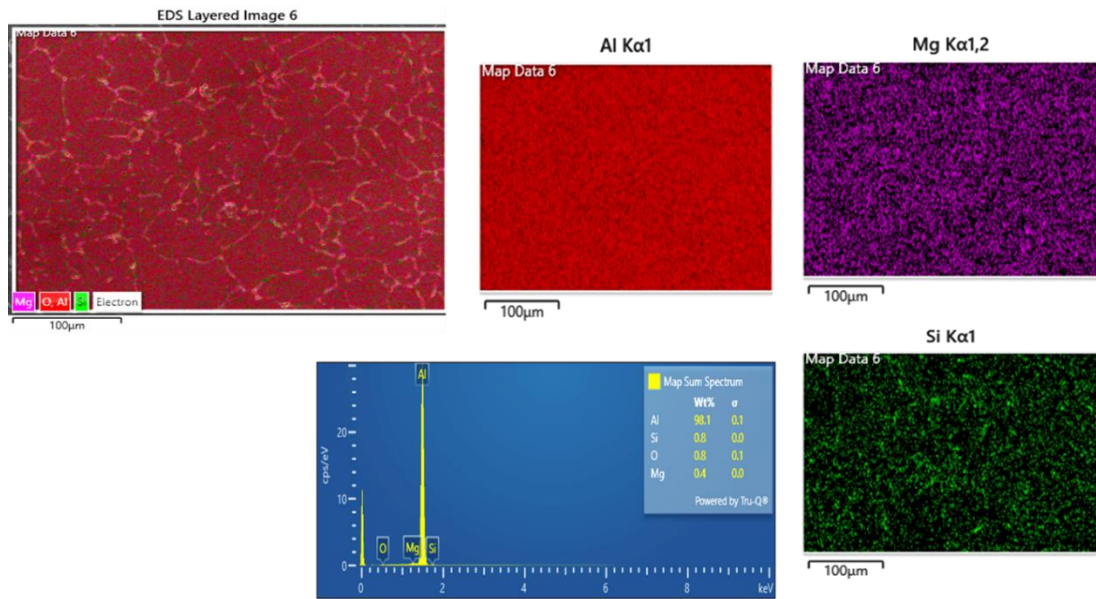
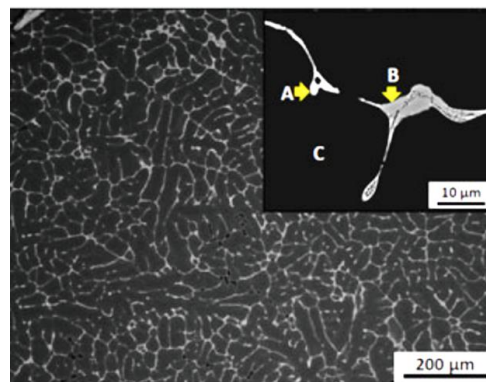


Figure 4.13 SEM-EDS area mapping of ZrTiO<sub>4</sub> added Al 7075.

The ZrTiO<sub>4</sub> added Al 7075 follows the same solidification pattern as shown in the as-cast microstructure.

Ghanghas et al. [300] experimented in situ dissolution of 7055 aluminium alloys and observed that the as-cast microstructure comprises α-Al solid solution with the secondary alloy phases found in the inter-dendritic channels (IDC). The IDC phases show up more clearly in BSE images and they are semi-continuous and spread out evenly in the alloy.



Phase	Al	Zn	Mg	Cu	Fe
A	37.88	31.24	12.13	18.75	–
B	58.14	3.93	–	20.30	17.63
C	90.43	7.72	1.85	–	–

Figure 4.14 BSE as-cast sample showing IDC (inter-dendritic channel) of 7055 with EDS analysis [300].

The micro-chemical analysis of the secondary phases is illustrated in Figure 4.14. The grey area points to  $Al_7Cu_2Fe$ , which is a Cu and Fe-bearing particle, whereas the brighter spots show either  $\eta$  or T with elements that possess a high atomic number such as Zn, Mg, and Cu.

### 4.3 Phase II: Effect of quenching medium on cast Al 7075

With the different quenching conditions, a permanent mold gravity die-cast is used to cast Al 7075. The three variants of casting Al 7075:

1. As-cast Al 7075 denotes by “as-cast”,
2. Ice quench denotes as “Ice”,
3. Quenched in hot water for 30 min denotes as “H30”, and
4. Quenched in hot water until cooled down denotes as “HTC”

There are a total of four experiments performed on cast Al 7075, and the comparison of microstructural and mechanical properties is studied.

#### 4.3.1 Microscopy of Phase II

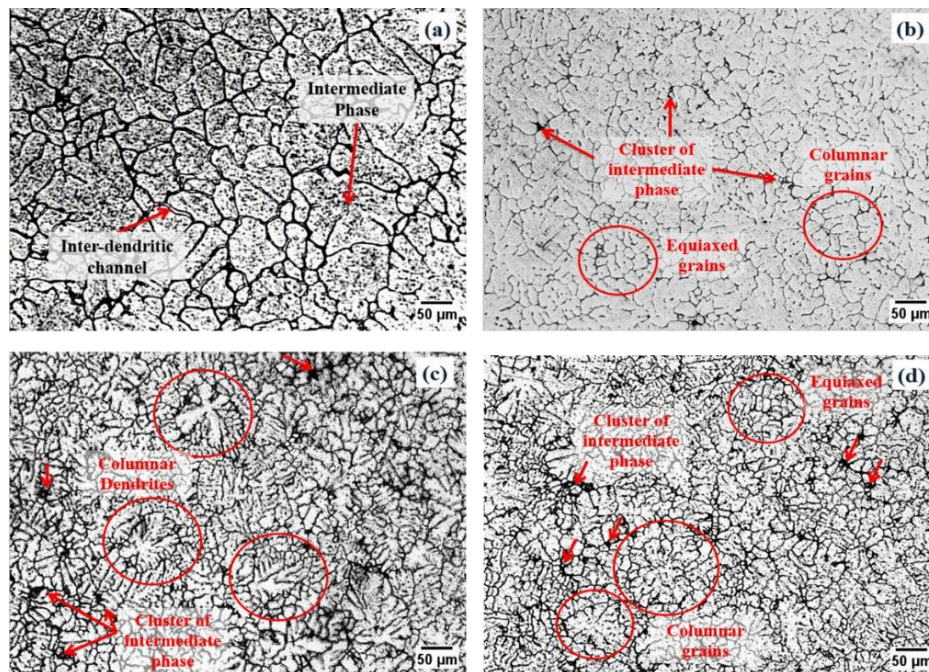


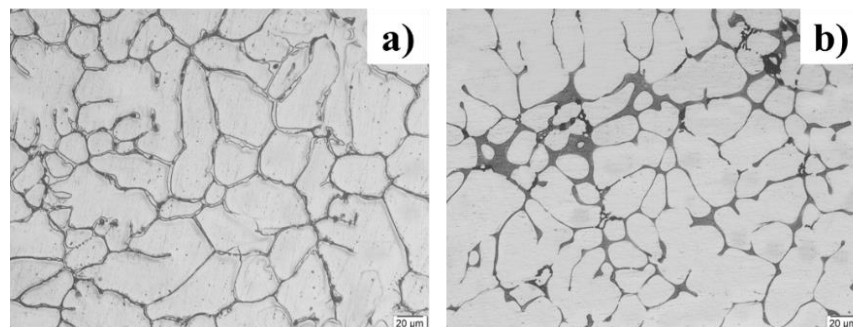
Figure 4.15 Optical micrographs of cast Al 7075 (a) as-cast, (b) ice quench, (c) hot water for 30 min, and d) hot water until cooled down.

Microstructural morphology is determined by the temperature of the mold wall, which is governed by mold diffusivity and conductivity, as well as the external driving force that quickly dissipates the heat outside of the mold. The heat that dissipates from the mold wall is varied by the quenching of ice and hot water here in this experiment. A slower cooling rate of  $10^2$  K/s provides a longer solidification time and results in the formation of coarser dendrite arms with larger dendritic arm spacing (DAS). A cooling rate of  $10^4$  K/s will lead to a shorter solidification time and form a finer dendrite with a lower DAS [301]. As shown in Figure 4.15 (a) to (d), cast Al 7075 is cooled by different quenching media, and compared with as-cast Al 7075.

The microscopic analysis of the as-cast material presents a combination of equiaxed and columnar  $\alpha$ -Al crystals. An inter-dendritic channel hosts the intermediate phases, as shown in Figure 4.15 (a). The mold wall, composed of cast iron with a thermal conductivity of around 32–35 W/mK, is cooled by ice. The rate of heat dispersion is very high, within the range of  $10^{10}$ - $10^{12}$  K/s, which is more likely to produce lower G/R ratios and resulting grain morphologies of equiaxed-columnar, as shown in Figure 4.15 (b). In between the equiaxed-columnar grain, the eutectic phase is solidified as a cluster. Due to the reduction in the heat dispersion in the case of hot water quenching for 30 minutes produces a higher G/R ratio, and finally, it reflects a coarse columnar dendritic microstructure, as shown in Figure 4.15 (c). In Figure 4.15 (d), the microstructure reveals coarse columnar dendrites with an equiaxed grain structure.

### 4.3.2 Natural ageing behaviour of cast Al 7075 by different quenching medium

The Al 7075 castings quenched with different quenching media are being subjected to a two-year time frame, similar to Phase I. The microstructural morphology is depicted in Figure 4.16 (a) to (d).



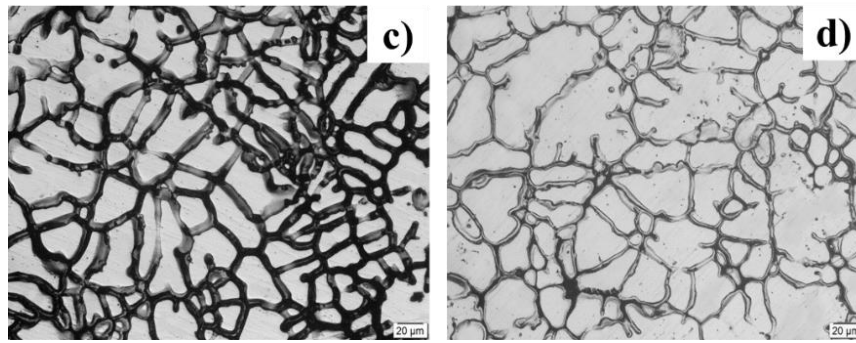
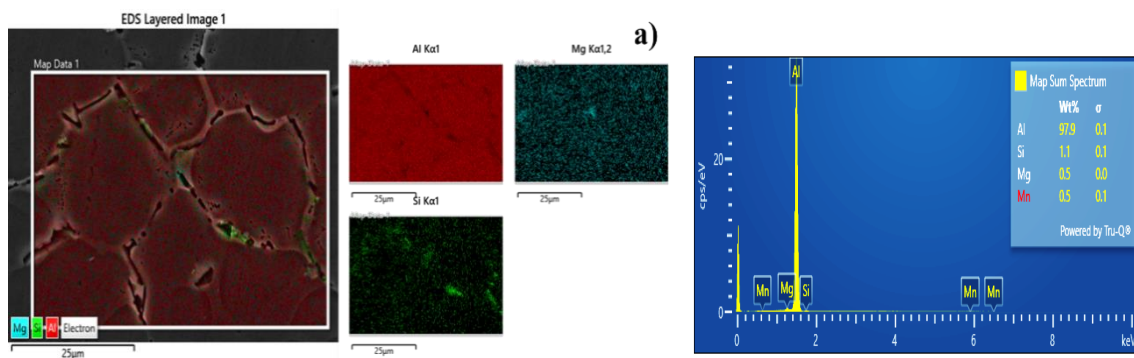


Figure 4.16 Micrographs of natural ageing of Al 7075 a) as-cast, b) ice quench, c) hot water for 30 min, and d) hot water until cooled down.

The secondary phases are precipitated at the grain boundary. As earlier mention, the as-cast Al 7075 microstructure is dissolved alloying elements. Matrix EDS mapping of the microstructure is captured with JEOL JSM 9600F to confirm an alloying element. The EDS mappings are shown in Figure 4.17 (a) to (d). The summary of elements is recorded in Table 4.8, and it is observed that  $\eta(\text{MgZn}_2)$  phase may form in the Ice and HTC system.

Table 4.8 Elemental mapping by EDS (wt.%)

System Al 7075	Elemental Mapping by EDS (Wt. %)					Ratio Zn/Mg	Closest phase
	Al	Si	Mg	Cu	Zn		
As-cast	97.9	1.1	0.5	--	--	--	--
Ice	90.0	--	2.0	1.9	6.1	3.05	$\eta(\text{MgZn}_2)$
H30	89.8	--	--	4.9	5.3	--	--
HTC	90.5	--	1.7	2.2	5.5	3.2	$\eta(\text{MgZn}_2)$



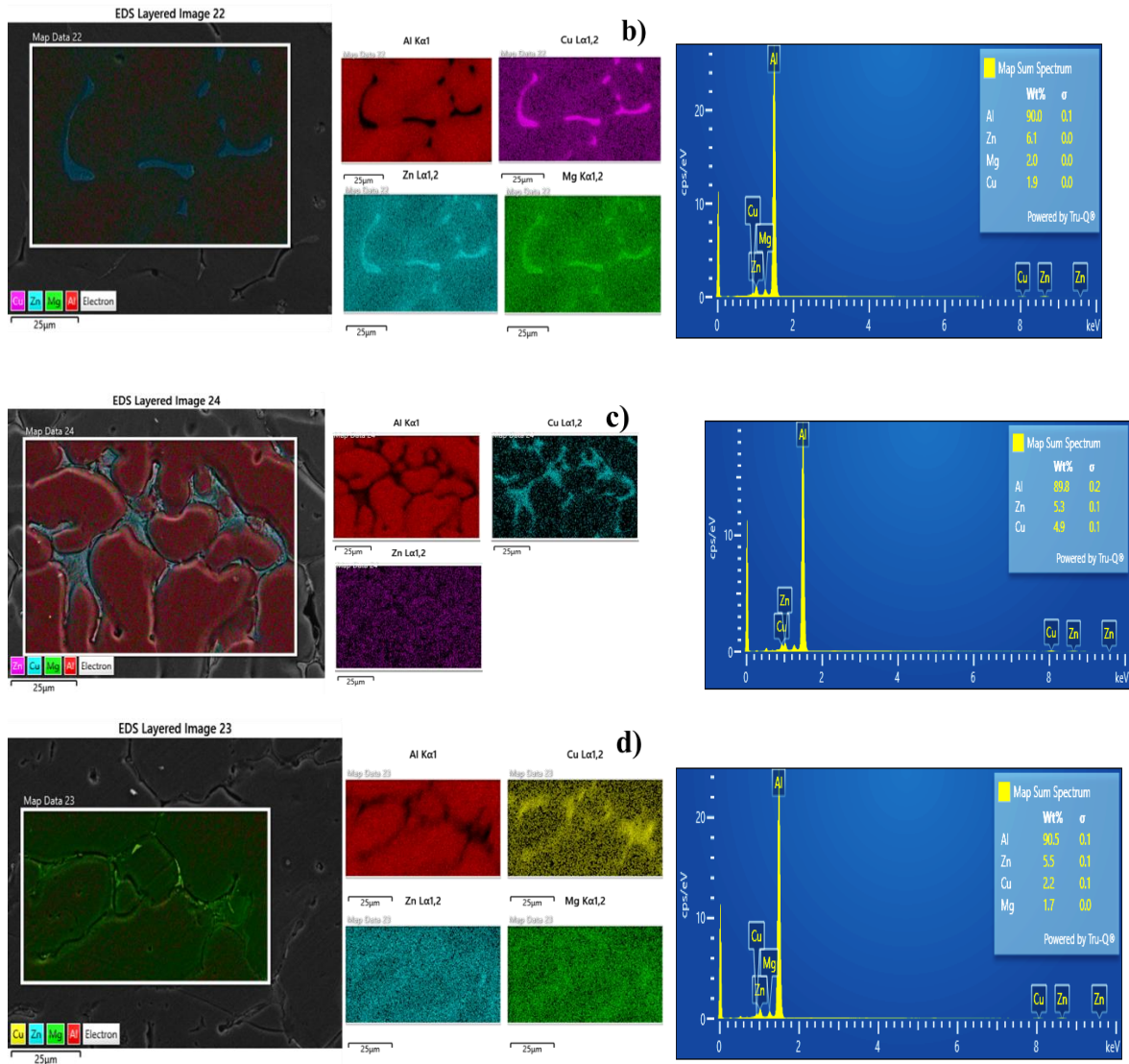


**Figure 4.17** Elemental mapped EDS layered images of Al 7075; a) as-cast, b) ice, c) H30, and d) HTC.

Guler et al. [302] studied a slope cooling of Al 7075 to get the non-dendritic structure and also got a higher copper concentration at the grain boundary. Similarly, the ice quenched sample shows the equiaxed-columnar microstructure compared to H30, and HTC samples. The dendritic and columnar dendrites are observed with the clustered solute segregation in H30 and HTC samples.

### 4.3.3 Mechanical properties of Phase II

The hardness values of all variants are compared, and it is found that the highest hardness is achieved in quenching in hot water until cools down, but after natural ageing, the highest

hardness is achieved for H30. The tensile strength values are more or less similar, and no significant difference is observed. The mechanical properties are presented in Table 4.9. The graphical presentation of mechanical properties is shown in Figure 4.18.

**Table 4.9 Mechanical properties of Al 7075; as-cast, quenched in ice, hot water for 30 min (H30), and hot water until cooled down (HTC).**

Mech. Properties	Alloy System (Quenching Media)			
	As-cast	Ice	H30	HTC
Hardness (BHN)	59	94	100	123
Hardness (BHN) (Naturally Aged)	89 (↑50.84%)	150 (↑59.57%)	164 (↑64.00%)	142 (↑15.44%)
Micro-hardness (HV <sub>0.5</sub> )	78	99	95	129
Micro-hardness (HV <sub>0.5</sub> ) (natural ageing)	82 (↑5.12%)	153 (↑54.54%)	172 (↑81.05%)	146 (↑13.17%)
Tensile Strength (MPa)	183	190	197	188
Elongation (%)	10	2	1.5	2

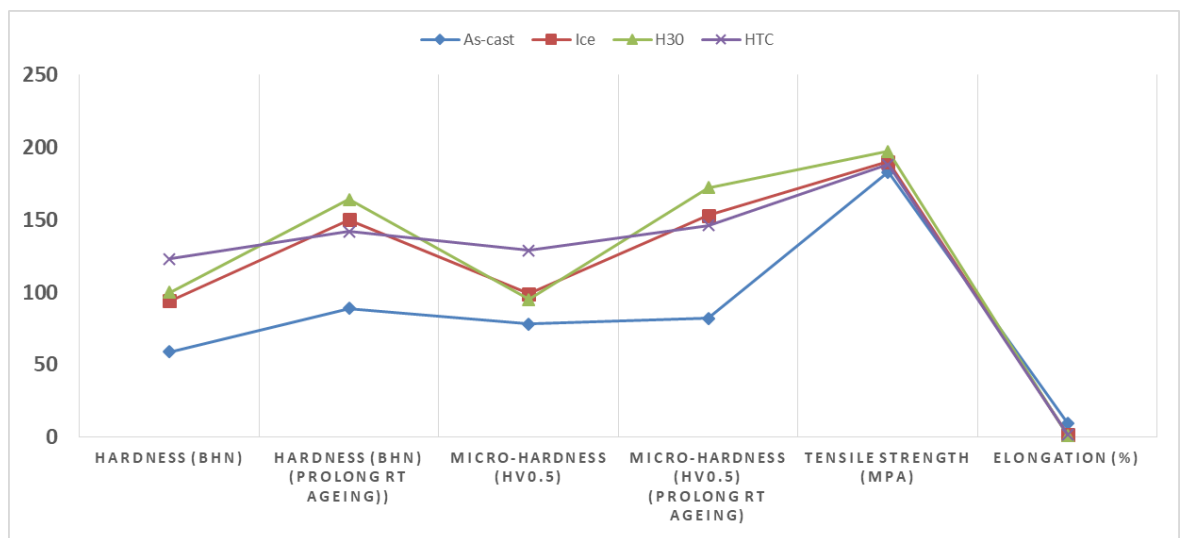


**Figure 4.18 Graphical presentation of as-cast and quenched Al 7075.**

#### 4.3.4 XRD analysis of Phase II

XRD analysis of as-cast Al 7075, and different quenching by ice, hot water for 30 min, and hot water until cools down are presented in Figure 4.19. The present intermediate phases in as-cast are Al<sub>0.95</sub>Mg<sub>0.05</sub>, and Al<sub>5</sub>Cu<sub>6</sub>Mg<sub>2</sub>. For the ice-quenched sample, Al-Mg, and Al-Cu-Mg phases are generated, and it is similar for H30, and HTC samples. The Mg<sub>1</sub>Zn<sub>2</sub> phase is formed in the H30, as shown in Figure 4.19.

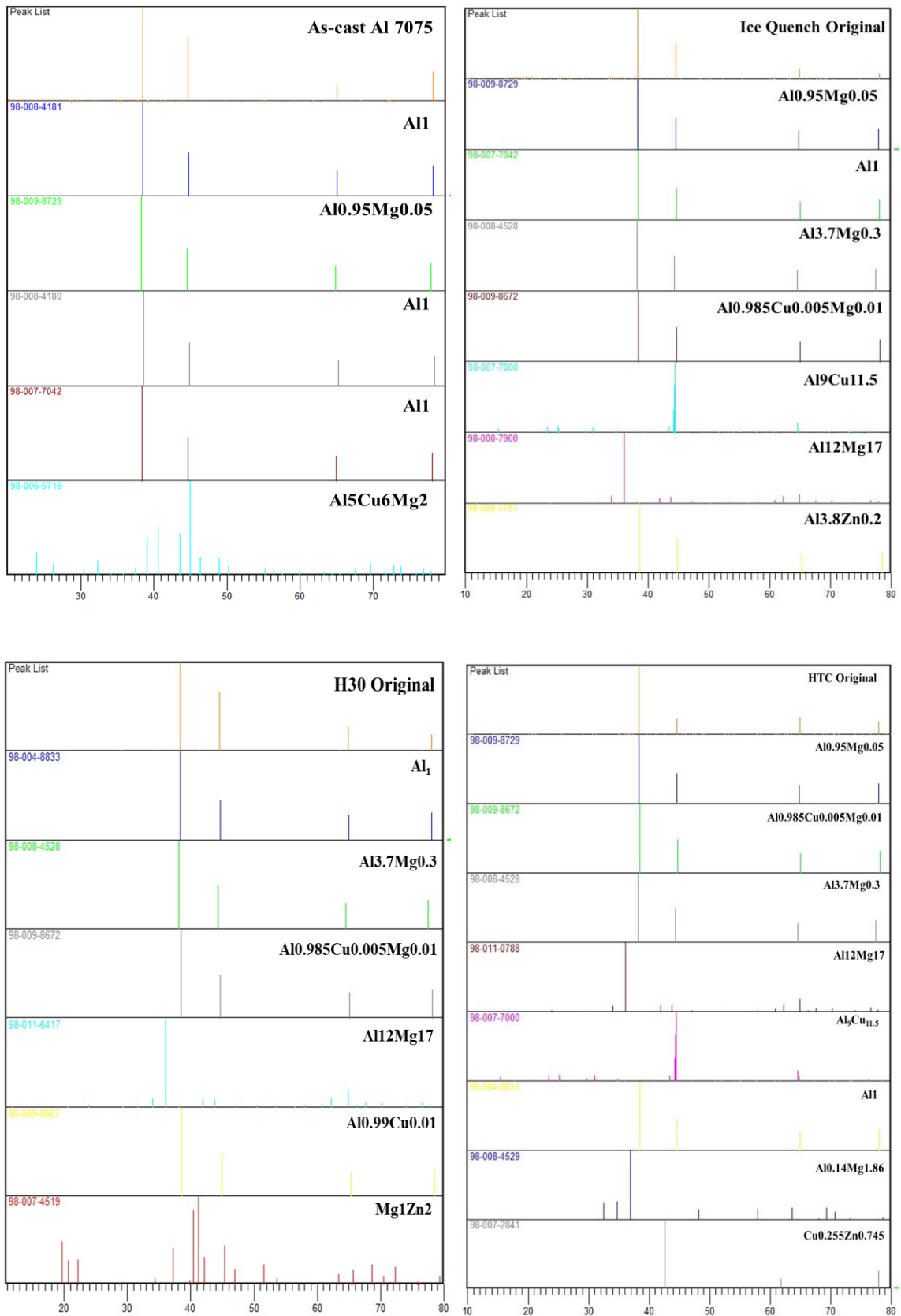


Figure 4.19 XRD plot for as-cast, ice, H30, and HTC quenched Al 7075.

4.3.5 Grain size measurement of Phase II

As shown in Table 4.10, the grain size of H30 samples is lower compared to others, i.e. 56.211  $\mu\text{m}$ . The grain size distribution is shown in Figure 4.20.

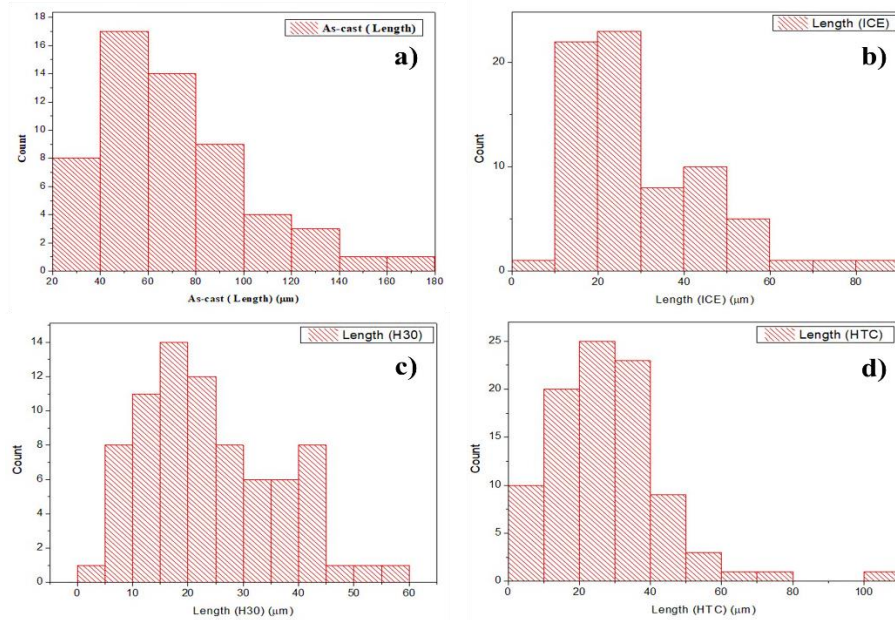


Figure 4.20 Grain size measurement of Al7075; (a) as-cast; and quenched (b) ICE; (c) H30; (d) HTC.

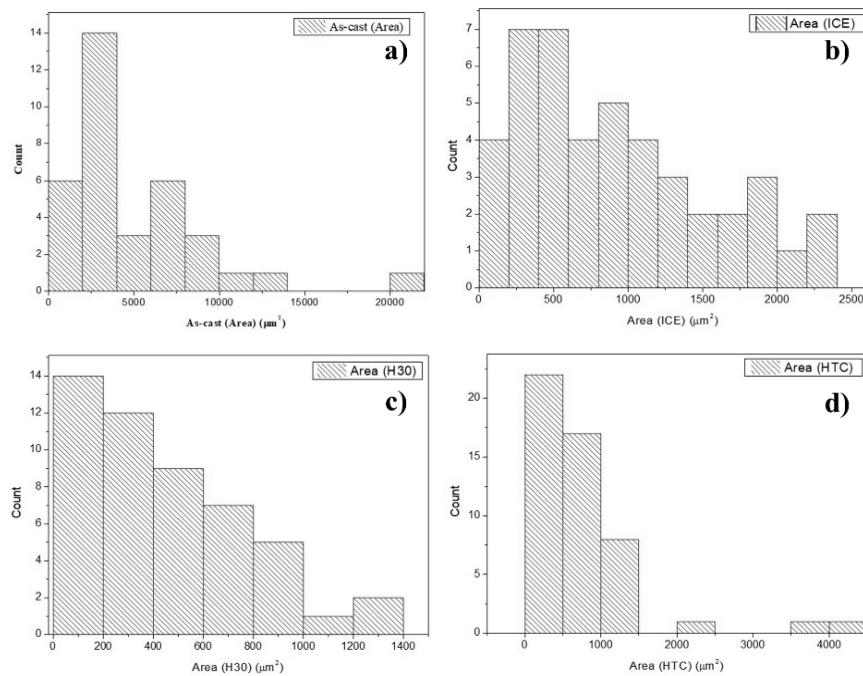


Figure 4.21 Grain area measurement of Al7075; (a) as-cast; and quenched (b) ICE; (c) H30; (d) HTC.

**Table 4.10** Min., max., and mean grain size and area of as-cast and quenched Al 7075.

System	Average Grain Length ( $\mu\text{m}$ )			Average Grain Area ( $\mu\text{m}^2$ )		
	Min.	Max.	Mean	Min	Max	Mean
As-cast	29.82	176.80	70.20	1257.74	21104.08	4987.71
ICE	37.07	82.79	139.49	876.89	4288.78	16394.44
H30	1.28	22.52	56.211	0.03	392.44	1338.66
HTC	5.98	24.09	100.78	50.77	520.57	4139.01

As shown in Figure 4.21, the graph of grain area distribution in the matrix is shown and found the small grain area distribution of the H30 sample. After natural ageing, there is an increment in hardness of 81.05%, compared to others.

#### 4.4 Phase III: Effect of double-step ageing on the oxide-added cast Al 7075

The  $\text{ZrO}_2$ ,  $\text{TiO}_2$ , and  $\text{ZrTiO}_4$  oxides are added individually in Al 7075, creating four alloy systems. These four systems are processed for double-step ageing, the following cycle is shown in Figure 4.22.

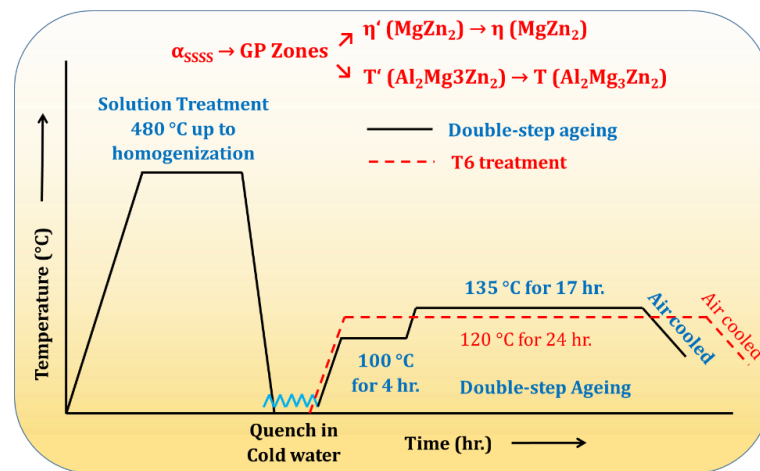


**Figure 4.22** Double-step ageing cycle for oxide-added cast Al 7075.

The solution treatment is given at 480 °C for 1h. and quenched in cold water. After that, double-step ageing is performed, 1<sup>st</sup> step at 100 °C for 4h, and 2<sup>nd</sup> step at 135 °C for 17 h. The motivation behind the double-step ageing is the early formation of GP zones, particularly GP I. By conventional T6, treatment at 120 °C for 24h achieved very good mechanical properties in wrought conditions. Zhang et al. [303] processed Al-5Mg-3Zn-1Cu (wt.%) cast alloy for double-step ageing at 120 °C for 1h followed by 150 °C for 4h, to

reduce the ageing time. Lubani et al. [304] homogenized AA 7075 samples by heating them to 470 °C for 2 hours and then quenching them in tap water. The double-step ageing process includes exposing samples to 150 °C for 2, 4, and 6 hours, followed by quenching. The same samples are aged at 185 °C for the same consecutive periods.

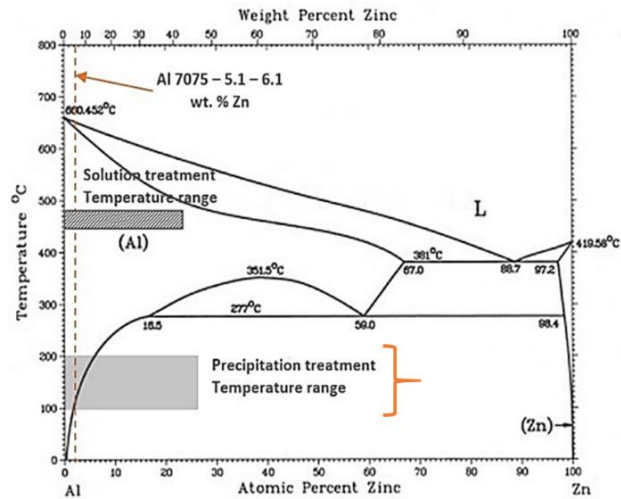


**Figure 4.23 Binary phase diagram of Al-Zn for a temperature range of solution treatment and precipitation treatment [305].**

The binary phase diagram of Al-Zn, as seen in Figure 4.23, outlines the temperature selection range for solution treatment and ageing treatment. The as-cast and oxide-added Al 7075 are characterised before and after the double-step ageing process. The following system nomenclature is used:

	System	Before double step ageing	After double step ageing
1	As-cast	AS	AS1
2	Al 7075/2.5 wt.% ZrO <sub>2</sub>	Z	Z1
3	Al 7075/2.5 wt.% TiO <sub>2</sub>	T	T1
4	Al 7075/2.5 wt.% ZrTiO <sub>4</sub>	ZT	ZT1

#### 4.4.1 Chemical analysis of cast Al 7075

A new set of heat is produced for this experiment. The oxides are added in Al 7075 for the double-step ageing process, and the chemical composition of the cast Al 7075 is shown in Table 4.11.

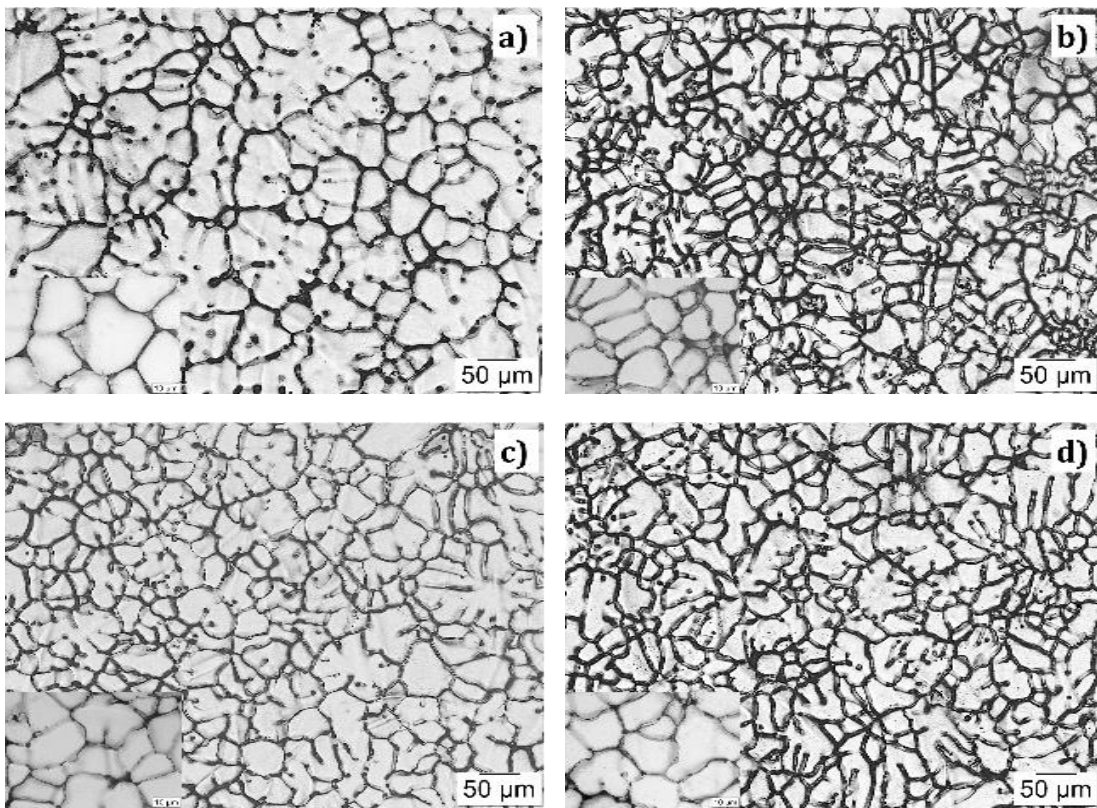
**Table 4.11** Chemical composition of as-cast Al 7075 for double-step ageing.

Alloy System	wt.%							
	Zn	Mg	Cu	Si	Cr	Ti	Zr	Balance
AS	5.72	2.42	1.8	0.07	0.2	0.001	0.005	89.784
Z	5.98	2.23	1.16	0.08	0.21	0.018	0.03	89.87
T	5.88	2.22	1.54	0.07	0.2	0.038	0.0103	90.06
ZT	6.06	2.28	1.67	0.08	0.2	0.027	0.0111	90.06

All the compositions are in the limit of Al 7075 after casting. The bulk proportion of Zr and Ti is limited in the sample.

**4.4.2 Microscopy of before and after the double-step ageing process**

The optical micrographs of all samples before and after heat treatment are shown in Figure 4.24 (a) to (d), and Figure 4.24 (e) to (h), respectively.



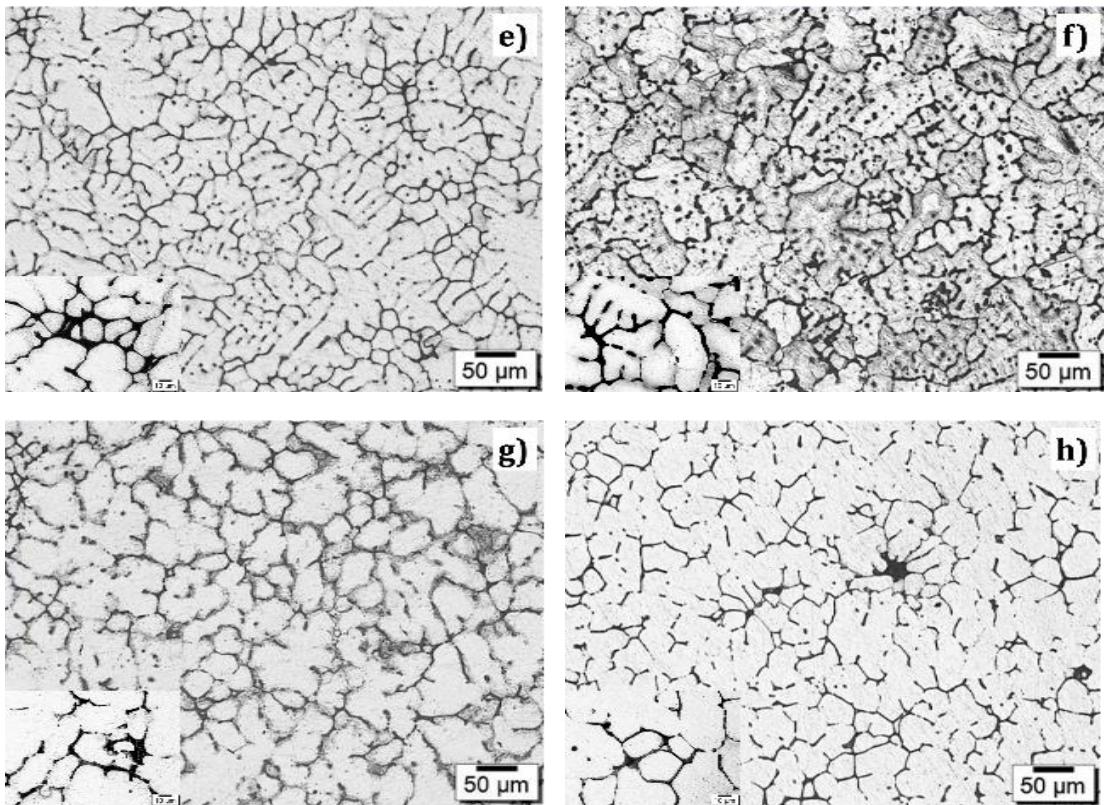


**Figure 4.24** Optical micrographs of oxide-added cast Al 7075 of as-cast,  $ZrO_2$ -added,  $TiO_2$ -added, and  $ZrTiO_4$ -added before heat treatment (a-d) and after heat treatment (e-h), respectively.

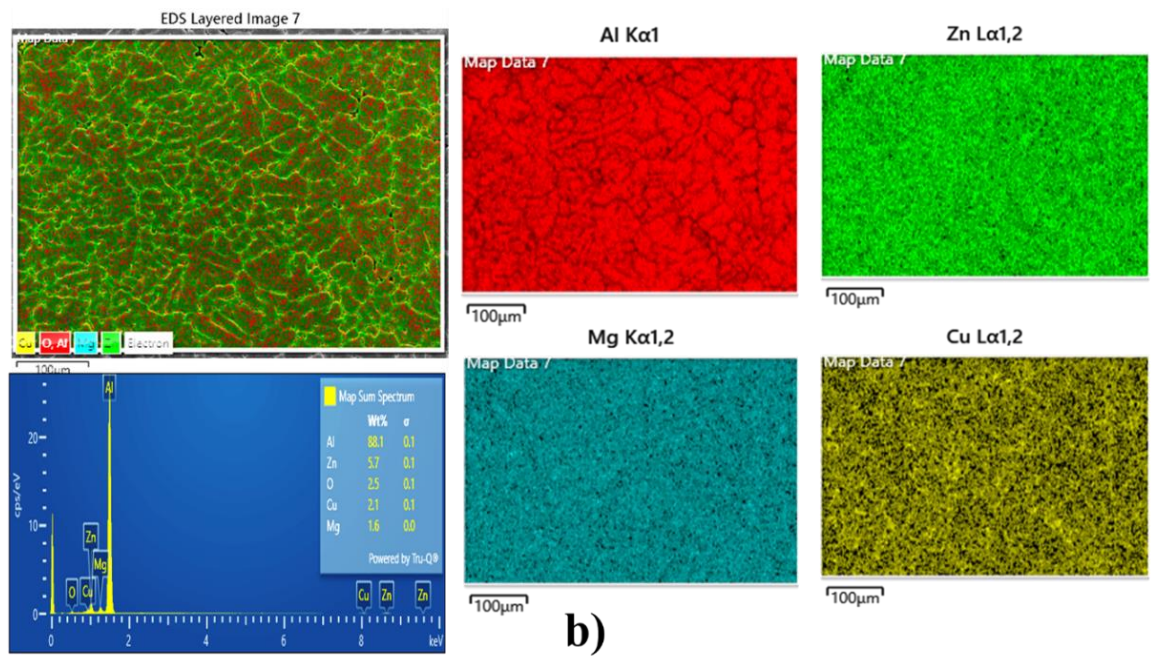
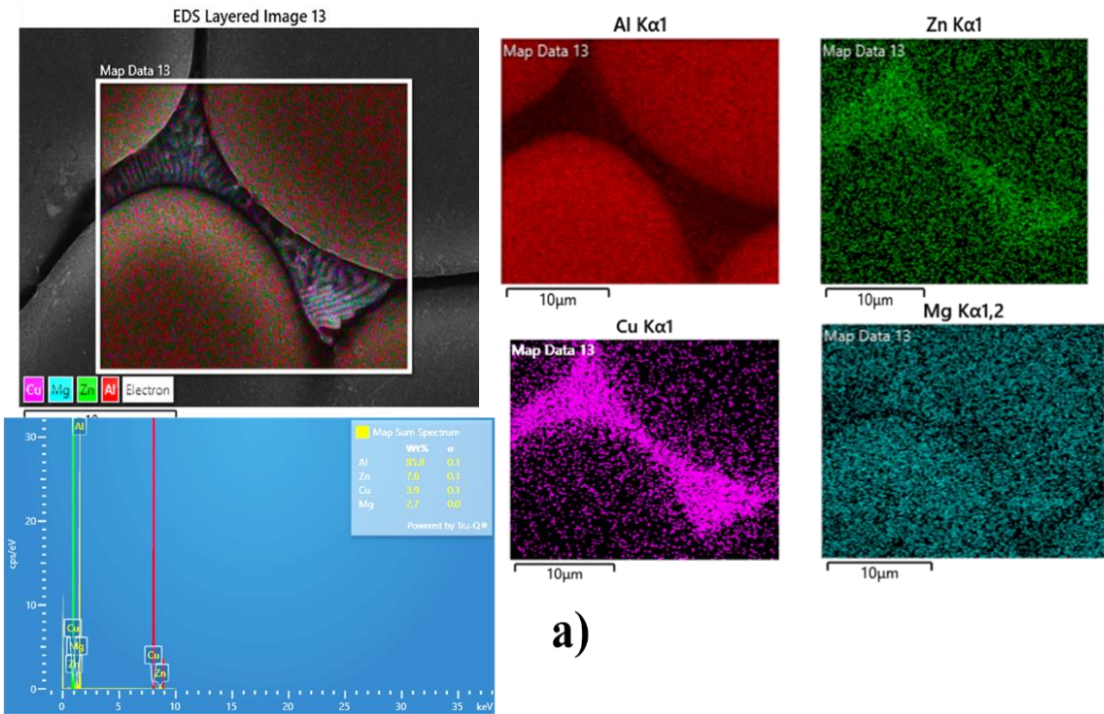
The as-cast micrograph shows the coarse size of  $\alpha$ -Al grains, as shown in Figure 4.24 (a). The eutectic phase is observed at the end of inter-dendritic grains. The primary cast structure presented  $\alpha$ (Al), a eutectic  $Mg(ZnCuAl)_2$  phase and  $Al_2Cu$  particles dispersed during casting. Severe dendritic segregation is present in this cast microstructure because of the chemical concentration gradient along the grain boundary. Figure 4.24 (b) shows the size reduction of  $\alpha$ -Al grains. The thick inter-dendritic boundaries are rich in the eutectic phase. The morphology of  $\alpha$ -Al changed from coarse equiaxed to fine columnar grains. There is also a presence of clustering of small equiaxed grains at a few locations. Figure 4.24 (c) shows thin inter-dendritic phases at the end of grains with a more uniform grain size of  $\alpha$ -Al observed. There is also the presence of sub-grains inside the grains, as well as the formation of coarse columnar grains. Figure 4.24(d) shows columnar dendrites significantly.

After the double-step ageing process, the effective precipitates are formed within the matrix of  $ZrO_2$  added Al 7075, as depicted in Figure 4.24 (e-h), compared to the others. Figure 4.24 (e) shows the micrograph of double-step aged as-cast Al 7075. The grain boundary

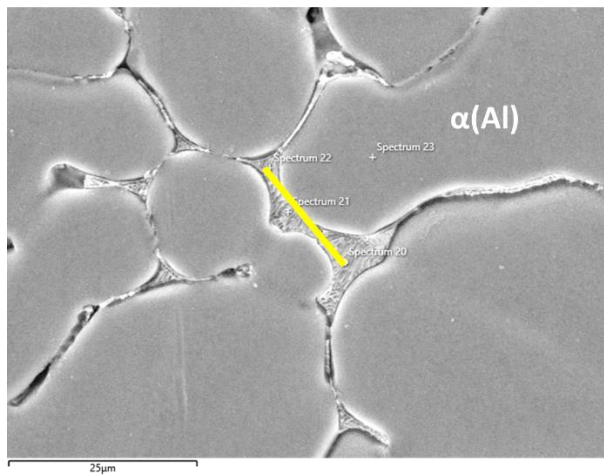
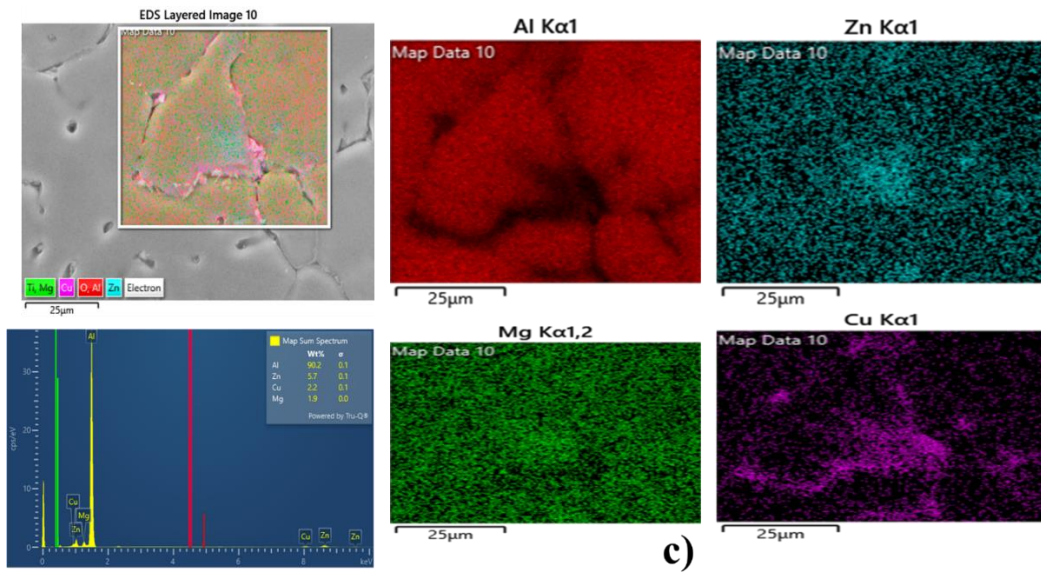
precipitates are formed at the triple point of the grain, and also grain boundary thinning is observed. Binesh and his colleagues [306] studied the strain-induced melt activation (SIMA) process of Al7075 and observed that intermetallic precipitates dissolve when heated isothermally, through the various transformations of  $\alpha\text{-Al} + \eta \text{ (MgZn}_2\text{)} \rightarrow \text{liquid phase (L)}$  and then from  $\alpha\text{-Al} + \text{Al}_2\text{CuMg (S)} + \text{Mg}_2\text{Si} \rightarrow \text{liquid phase (L)}$ . Gosh et al. [254] investigated and found that the homogenisation process reduced the dendritic network structure and area fractions of the eutectic phase. Homogenisation at 465°C for 96 hours caused intermetallic phases to be dissolved into the matrix, which agreed with the homogenisation kinetic analysis. Figure 4.24 (f) there is a very fine spread of precipitates throughout the  $\alpha(\text{Al})$  matrix, and Li et al. found that introducing Zr to 7xxx alloys results in a finer grain structure and a decrease in recrystallization by forming dispersed particles, i.e.  $\text{Al}_3\text{Zr}$  for Zr-containing alloys. Priya et al. [307] studied post-homogenisation cooling and precipitates particle size distribution model. The precipitates are classified into three classes: high, medium, and low temperature. Cooling to temperatures below 200 °C and the corresponding saturation and diffusion causes precipitation of the T and  $\eta$  phases (solvus temperatures 174 °C and 80 °C for Al-6Zn-2Cu-2Mg-0.13Zr, respectively). The equal distribution of precipitates improves the mechanical properties of the alloy. Luo et al. [308] investigated the pre-ageing behaviour of Al-Zn-Mg-Cu and determined that pre-ageing treatment at 100 °C increases the hardness of the product because of an increase in dislocation density. Figure 4.24 (g) shows the micrograph of  $\text{TiO}_2$  addition increases the potency of the nucleation site resulting in uniform distribution of the second phase. Figure 4.24 (h) shows  $\text{ZrTiO}_4$  added Al 7075, the interdendritic channel and continuity of grain boundary broken, and dispersion of the eutectic phase is observed.

#### *4.4.2.1 Elemental mapping of oxide-added Al 7075 (before and after ageing)*

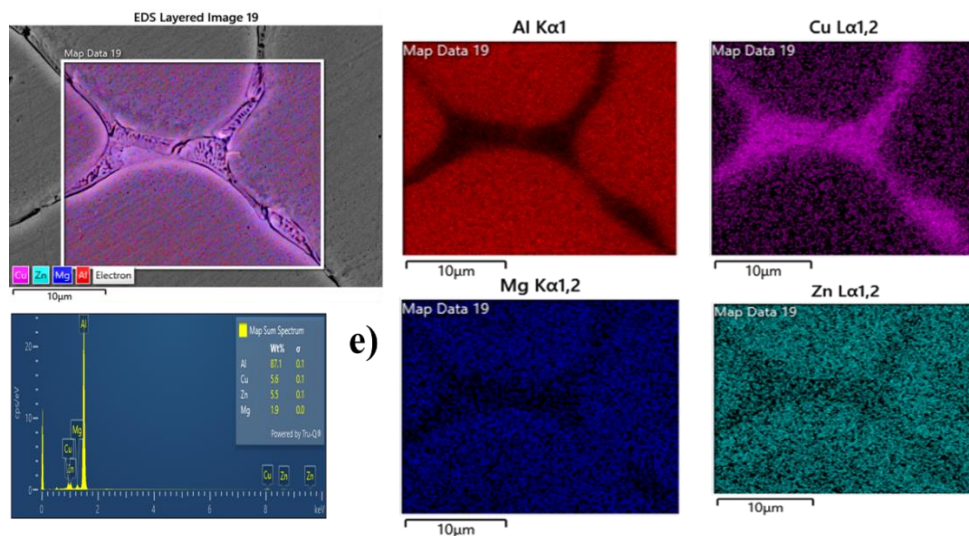
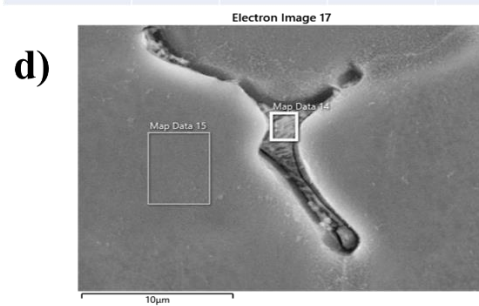
The elemental mapping of as-cast and oxide-added Al 7075 is presented in Figure 4.25 (a) to (h).



# Results and Discussion



Spectrum	Al	Zn	Mg	Cu
20	48	10.8	7.4	33.8
21	44.4	12.7	9.4	33.5
22	77.5	9.3	3.3	9.9
23	93.9	4.7	1.4	--



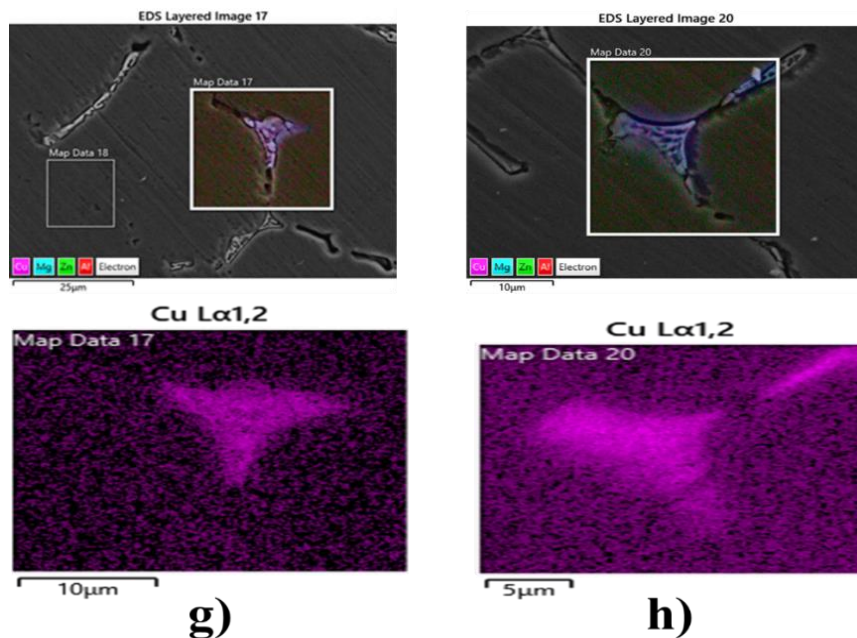
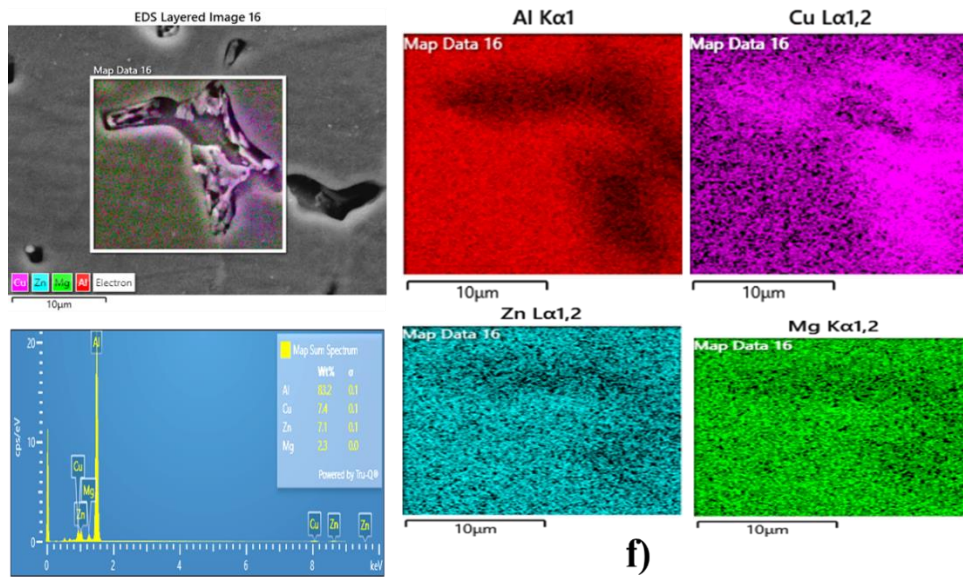


Figure 4.25 Elemental mapping of as-cast and oxide added Al 7075 (a–d) before double-step ageing, and (e–h) after double-step ageing.

As represented in the above mapping, the elements are more likely to segregate at the grain boundary rather than within the grain. For the segregation of solute elements, Liu et al. [41] environment-sensitive embedding energy from found that for a large value of environment-sensitive embedding energy, more solute atoms are influenced by the surrounding environment, becoming unstable and diffusing to the stable environment where this energy is low [309].

$$E_{ESE} = [E_i - (n - 1) E_{self} - E_{iself}] - (E_{cl} - nE_{self})$$

$E_i$  is the structural energy with a solute atom,  $E_{cl}$  is the structural energy without a solute atom,  $n$  denotes atomicity,  $E_{self}$  is the matrix atomic energy, and  $E_{iself}$  is the matrix-solute atomicity energy. The calculated environment-sensitive embedding energies for Zn, Mg, and Cu are stated in Table 4.12.

**Table 4.12 Environment-sensitive embedding energy of Zn, Mg, and Cu at the grain boundary and  $\alpha$ -Al** <sup>[309]</sup>.

Position	Zn	Mg	Cu
At grain boundary	1.6452	21.9444	22.6892
In $\alpha$ -Al	1.1292	22.5959	23.0077

From the above table, the environment-sensitive embedding (ESE) energy of Zn in the  $\alpha$ -Al grain matrix is lower than the grain boundary, so Zn atoms are distributed uniformly within the matrix. While ESE of Mg and Cu is higher than Zn atoms within the  $\alpha$ -Al matrix, so lower solid solubility. Hence, Mg and Cu atoms are found at grain boundaries. Cu has the highest ESE in the  $\alpha$ -Al matrix, so solid solubility is to be the least <sup>[41]</sup>. Hence, the same pattern of segregation is followed in the above elemental mapping, as shown in Figure 4.25.

#### 4.4.3 XRD analysis of Phase III

XRD analysis of oxide-added samples before the ageing process is shown in Figure 4.26, and after the double-step ageing process is shown in Figure 4.27. Before the ageing process, in as-cast,  $Al_{0.95}Mg_{0.05}$ ,  $Al_4Cu_9$ ,  $Al_{4.2}Cu_{3.2}Zn_{0.7}$ , and  $Mg_1Zn_2$  phases are present. In  $ZrO_2$ ,  $Al_{3.8}Zn_{0.2}$ ,  $Al_{3.7}Mg_{0.3}$ ,  $Al_{0.98}Zr_{0.02}$ ,  $Mg_1Zn_2$ ,  $Al_3Zr_1$ , and  $Mg_{3.946}Zn_{21.336}Zr_{1.149}$  phases are present. Similarly, For  $TiO_2$ ,  $Ti_1$ ,  $Al_{3.7}Mg_{0.3}$ ,  $Al_{3.8}Zn_{0.2}$ ,  $Al_1Cu_2Ti_1$ ,  $Al_{0.93}Cu_{1.07}Mg_1$ ,  $Cu_2Mg_1$ ,  $Cu_1Ti_1$ , and  $Al_1Cu_1Mg_1$  phases are present, which are more copper-rich. With  $ZrTiO_4$ ,  $Al_{0.95}Mg_{0.05}$ ,  $Al_{0.98}Zr_{0.02}$ ,  $Ti_1Zr_1$ ,  $Al_3Ti_1$ ,  $Al_{35.472}Cu_{47.792}$ , and  $Cu_2Zn_1Zr_1$  phase are present.

Figure 4.27 shows the XRD analysis of as-cast, oxide-added samples. The intermediate phases are stated in the peak list similar to before ageing treatment samples. The formation of  $MgZn_2$  is common in the  $ZrO_2$ , and  $TiO_2$  added samples after ageing.

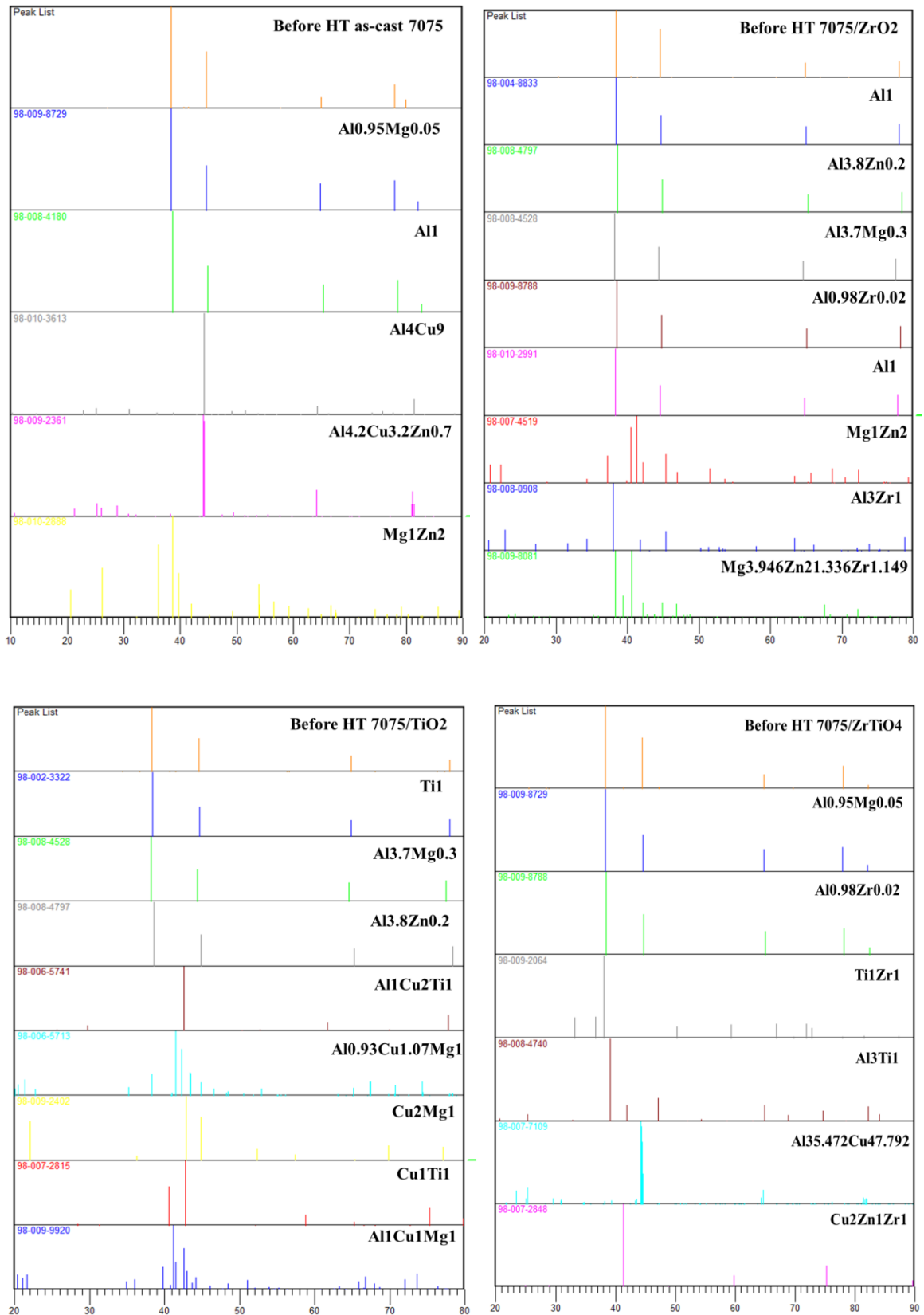


Figure 4.26 XRD analysis of as-cast and oxide added Al 7075 before ageing treatment.

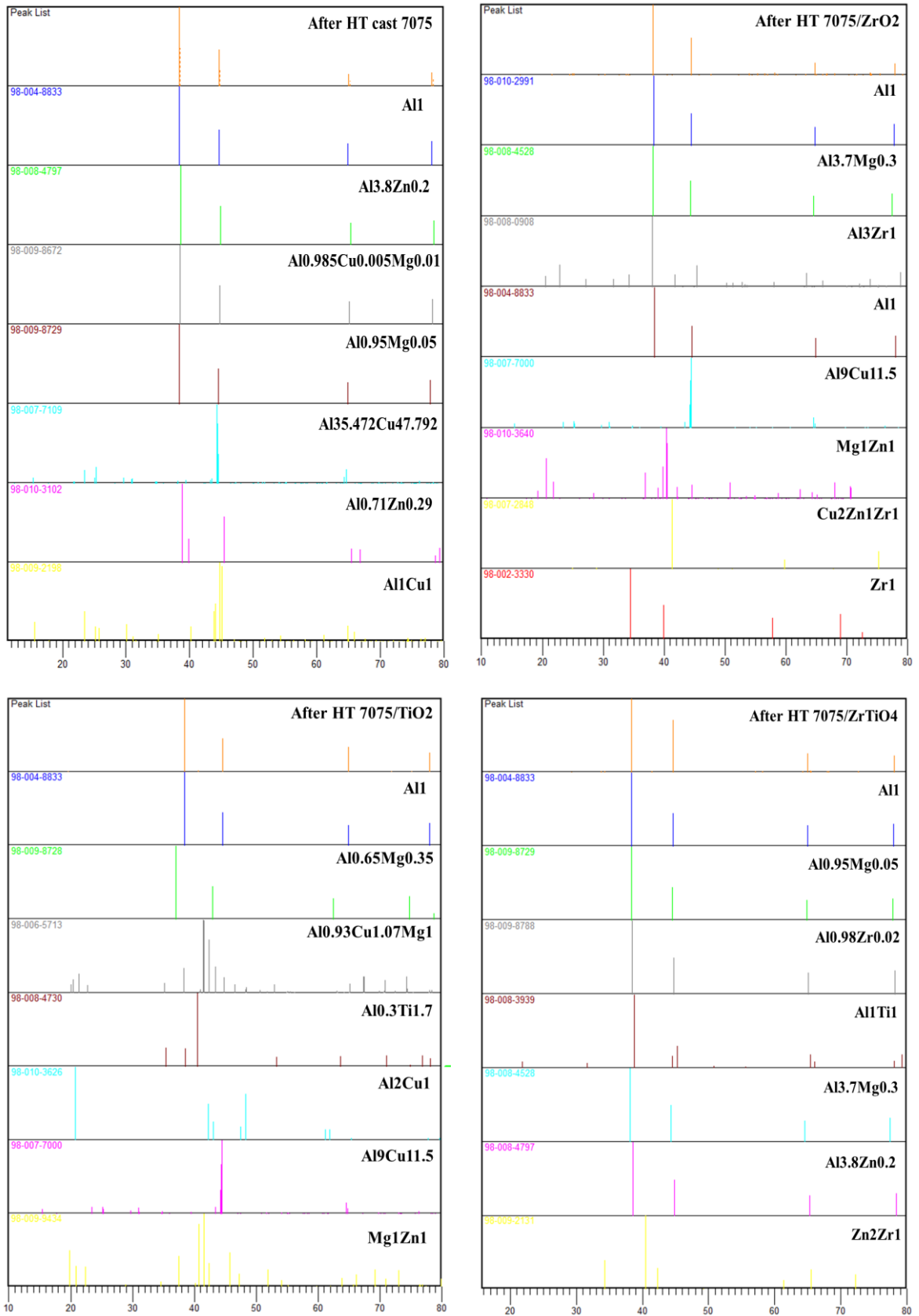


Figure 4.27 XRD analysis of as-cast, oxide added Al 7075 after ageing treatment.

#### 4.4.4 Mechanical Properties of Phase III

The tensile testing, hardness and micro-hardness testing are done on all the samples to determine their mechanical properties. The mechanical properties of oxide-added cast Al 7075 are presented in Table 4.13. The mechanical properties of Al 7075 improved before and after ageing treatment with the addition of ZrO<sub>2</sub>. The mechanical properties are improved due to the even distribution of precipitates within the matrix and the reduction of precipitates at the grain boundaries. After ageing treatment, the same pattern is seen for samples with TiO<sub>2</sub> and ZrTiO<sub>4</sub> added. An increase of 72% in tensile value and 53% in hardness value was seen, however, not much of a difference was noted in the micro-hardness value of samples containing ZrO<sub>2</sub>. After ageing treatment, a decrease in micro-hardness is seen in as-cast, TiO<sub>2</sub>, and ZrTiO<sub>4</sub>-added samples.

**Table 4.13 Mechanical properties of as-cast, ZrO<sub>2</sub>-added, TiO<sub>2</sub>-added, and ZrTiO<sub>4</sub>-added cast Al 7075 before and after ageing treatment.**

Mech. Properties	Before HT				After HT			
	AS	Z	T	ZT	AS1	Z1	T1	ZT1
Hardness (BHN)	106	104	99	105	111 (↑4.71%)	160 (↑53.84%)	146 (↑47.47%)	140 (↑33.33%)
Micro-hardness (HV <sub>0.5</sub> )	147	144	136	129	114 (↓22.44%)	171 (↑18.75%)	155 (↓13.97%)	111 (↓13.95%)
UTS (MPa)	147	212	189	184	279 (↑89.79%)	366 (↑72.64%)	317 (↑67.72%)	293 (↑59.23%)
Elong. (%)	2	2	2.5	3	2	1.5	1.5	1.5

#### 4.4.5 Grain size measurement of Phase III

The grain size should remain unaffected by double-step ageing. So, the grain size is measured before ageing treatment and is represented in Figure 4.28.

In Figure 4.28, the grain size measurement reveals that the grain size distribution of the ZrO<sub>2</sub> added sample is significantly smaller than the other samples. The grain area observed in ZrO<sub>2</sub>, TiO<sub>2</sub>, and ZrTiO<sub>4</sub> added samples is nearly identical, as shown in Figure 4.29. Hence, the mechanical properties of the oxide-added sample are significantly higher than the as-cast.

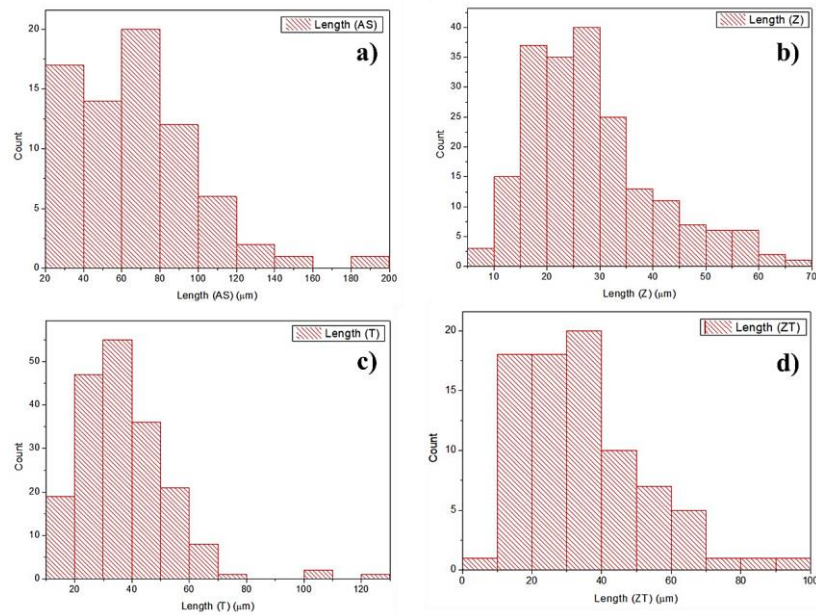


Figure 4.28 Grain size measurement of as-cast and oxide added Al 7075.

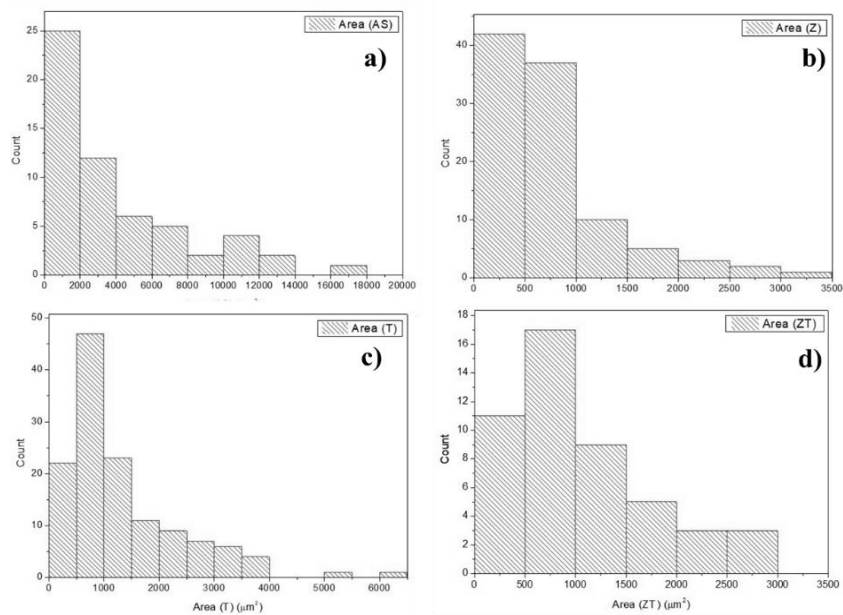


Figure 4.29 Grain area measurement of as-cast and oxide added Al 7075.

#### 4.4.6 Tribology of Phase III

Tribology research is done on samples with as-cast,  $\text{ZrO}_2$ , and  $\text{TiO}_2$  included. This experiment does not consider  $\text{ZrTiO}_4$  added samples to save time and simplify the data. Wear is a material loss of a solid surface when materials are in contact with surfaces, as they are in relative movement [310]. Wear occurs through surface interactions at the asperities. When

two bodies are in relative movements, and the asperities come in contact, friction is generated at the asperities level and induced materials losses <sup>[311]</sup>. When the load increases, the chances of friction also increase. Thus, wear is not a material property but a system property. Hence, wear depends on the materials, operating parameters, and environmental conditions. There are two types of relative movement: sliding and rolling; out of both, sliding movement is more dominating.

### 4.4.6.1 Sliding wear operating parameters

In the experiment, a DUCOM pin-on-disc type tribometer is used with counterformal or concentrated contact, typically occurring at a point or line. At a point of contact, higher stresses are generated under a load with higher intensity. The sliding for metallic materials has plastic deformation and oxidative wear, while ceramics and composites have brittle fracture and tribochemical effects <sup>[310]</sup>. Finally, wear losses as a function of operating conditions, types of materials, and system design. The operating parameters used during testing and their results are presented in Table 4.14.

The wear rate can be calculated as a specific wear rate by the below equation.

$$W_{sp} = \frac{V}{L * D} \left( \frac{mm^3}{N - m} \right)$$

Where V, L, and D are the total volume of wear, the normal load, and the sliding distance, respectively. The operating parameters are sliding distance, rotational speed, and applied normal load. Out of three, the sliding distance is constant for all wear tests. Table 4.14 shows the result of the wear weight losses and volume losses data. The weight and volume losses offer a more convenient way to explain the material's performance compared to the wear rate for different alloy systems. By increasing the applied load from 10 to 50 N and rotational speed from 500 to 1000 rpm, the scar diameter increased from 2.75 mm to 6.70 mm with as-cast samples. Similarly, the same phenomena were observed in the ZrO<sub>2</sub> and TiO<sub>2</sub>-added samples. The ZrO<sub>2</sub>-added sample showed minimum and maximum scar diameters of 1.50 mm and 5.55 mm, respectively. The TiO<sub>2</sub>-added sample showed minimum and maximum scar diameters of 2.10 mm and 5.80 mm, respectively. The scar diameters decreased in both oxides added samples.

**Table 4.14 Operating parameters for tribology of AS, Z, and T samples at various applied loads and rotational speed with recorded weight and volume loss with scar diameter.**

Test Condition					Specimen Material		
Normal load in N		10, 20, 30, 50 (For all specimens)			<b><u>Stationary pin: Ø 8 mm</u></b>		
The rotational speed of the disc in rpm		500, 700, 100 (For all specimens)			1. Al 7075 as-cast (AS)		
Time in sec		1274@500 rpm 910@700 rpm 634@100 rpm			2. 2.5 wt.% ZrO <sub>2</sub> added Al7075		
Sliding distance in meter (Sliding distance = circumference*rpm*time)		1000 m (fixed)			3. 2.5 wt.% TiO <sub>2</sub> added Al7075		
Wear track dia. in mm		30 mm			<b><u>Rotating Disc:</u></b> EN31 hardened to 62 HRC		
					<b><u>The density of Al 7075 pin:</u></b> 2.81 g/cc		
Alloy system	Rotational speed in rpm	Frictional force in N	Cof	Time in sec	Wt. loss in gm	Vol. loss in mm <sup>3</sup>	Scar dia. in mm
AS	500	6.83	0.37	1274	0.0009	0.32	2.75
		12.74	0.44		0.0060	2.14	3.50
		13.26	0.64		0.0259	9.22	4.03
		18.65	0.68		0.0390	13.88	5.06
	700	6.25	0.37	910	0.0013	0.46	3.01
		13.20	0.44		0.0075	2.67	5.00
		12.95	0.65		0.0184	6.55	5.08
		18.72	0.63		0.0279	9.93	6.10
	1000	6.75	0.38	634	0.0037	1.32	4.02
		13.91	0.46		0.0312	11.10	5.92
		13.80	0.69		0.0444	15.80	6.20
		19.10	0.68		0.0607	21.60	6.70
Z	500	6.20	0.37	1274	0.0017	0.60	1.50
		12.84	0.44		0.0059	2.10	3.15
		13.24	0.64		0.0094	3.35	3.00
		18.67	0.62		0.0123	4.38	3.20
	700	6.14	0.37	910	0.0025	0.89	2.00
		13.46	0.45		0.0083	2.95	4.50
		13.52	0.67		0.0128	4.56	5.00
		18.67	0.61		0.0228	8.11	5.10
	1000	6.32	0.39	634	0.0022	0.78	2.20
		13.25	0.45		0.0136	4.84	5.02
		13.54	0.66		0.0208	7.40	5.50
		19.25	0.63		0.0314	11.17	5.55
T	500	6.67	0.38	1274	0.0006	0.21	2.10
		13.54	0.45		0.0046	1.64	3.20
		13.44	0.68		0.0040	1.42	3.96
		18.96	0.67		0.0028	1.00	3.50
	700	6.85	0.38	910	0.0032	1.14	2.30
		13.69	0.46		0.0095	3.38	4.60
		18.88	0.68		0.0136	4.84	4.90
		13.81	0.69		0.0189	6.73	5.60
	1000	6.91	0.39	634	0.0025	0.89	4.20
		14.12	0.47		0.0215	7.65	5.10
		13.74	0.69		0.0246	8.75	5.60
		19.58	0.69		0.0314	11.17	5.80

The weight loss is calculated for the applied load of 10, 20, 30, and 50 N for the three types

of samples at 500, 700, and 1000 rpm speed. The graphical representation of results is shown in Fig. 6. At 500 rpm, for as-cast Al7075, the wear rate increases with an increase in load from 10 to 50 N. Metals offer maximum plastic deformation while loading at higher speeds generates maximum temperature because of friction, maximizing material loss from the surfaces. For applied normal load 10-50 N and 500, 700, and 1000 rpm speeds, the weight loss percentage range from 0.020 wt.% to 1.027 wt.% for as-cast, 0.0389 wt.% to 0.5534 wt.% for ZrO<sub>2</sub>, and 0.0142 wt.% to 0.5556 wt.% for TiO<sub>2</sub>-added sample.

As shown in Figure 4.31 (a) and Figure 4.31 (b), the SEM images had ploughing lines throughout the sliding direction. The ploughing line with deeper wear marks is observed. In oxide-added samples, the wear is significantly lesser than the as-cast.

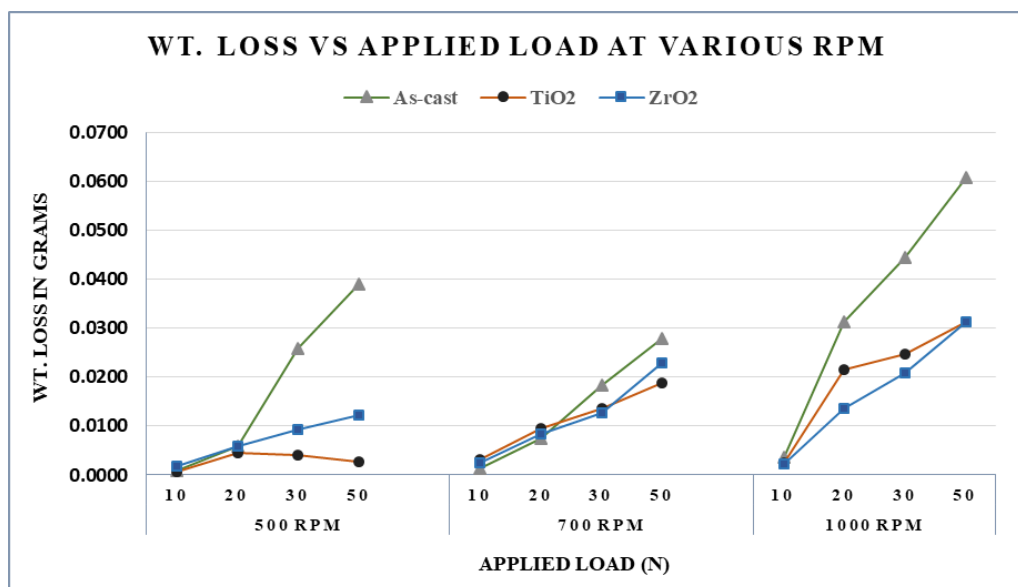


**Figure 4.30** Wear analysis of as-cast, 2.5 wt.% ZrO<sub>2</sub> added and 2.5wt.% TiO<sub>2</sub> added Al7075 at 500, 700, and 1000 rpm at 10, 20, 30, and 50 N applied loads, respectively.

As shown in Figure 4.30, the graph trend of the oxide-added samples is lower than the as-cast with the same parameters. It is because of the presence of oxides responsible for creating a barrier between the sliding of samples and the hard disc. The sliding speed increase wears loss also increases, and it is reported up to 1000 rpm in all the cases. SEM analysis of the worn test sample was carried out to study the effect of different applied loads and speeds. Figure 4.31 (a) & (b) show wear surfaces of as-cast Al7075. Figure 4.31 (c) & (d) show 2.5 wt.% ZrO<sub>2</sub> added sample and Figure 4.31 (e) & (f) show 2.5 wt.% TiO<sub>2</sub> added sample.

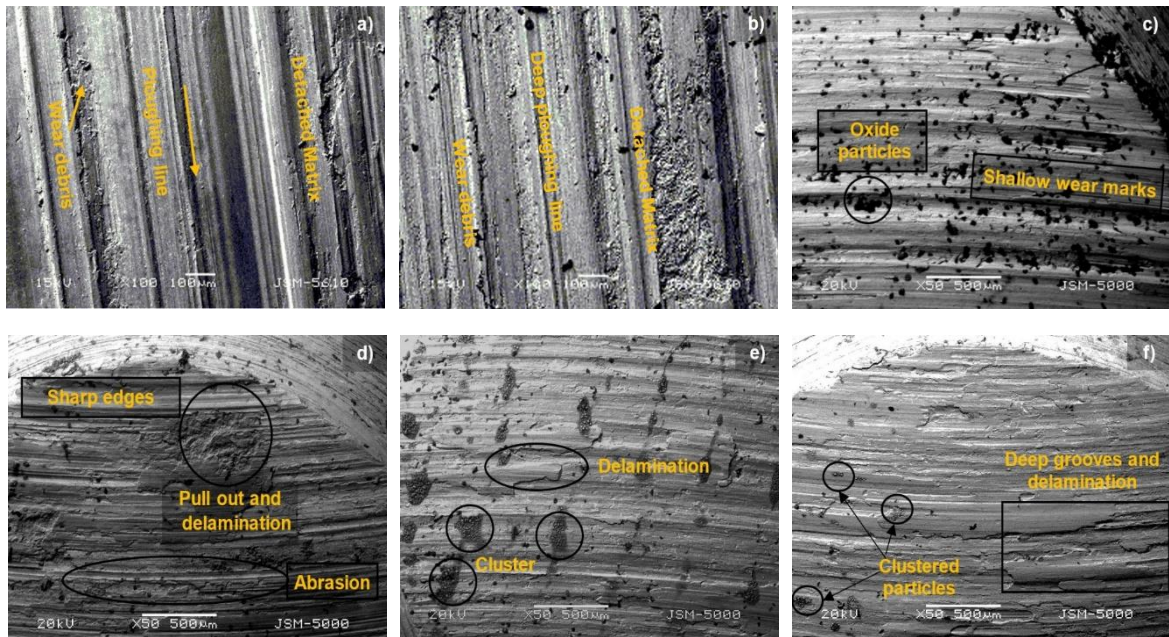


**Figure 4.31 Surface Morphology of wear samples of Al 7075 at 1000 rpm at 10 N load a) as-cast, c) ZrO<sub>2</sub> added Al7075, and e) TiO<sub>2</sub> added Al7075; at 50 N load, b) as-cast, d) ZrO<sub>2</sub> added Al7075, and f) TiO<sub>2</sub> added Al7075.**

Oxide-added samples revealed abrasive and adhesive wear mechanisms with delamination and shallow wear marks. Al 7075, in its as-cast state, was seen with more prominent wear tracks and grooves because of high abrasion.

#### 4.5 Phase IV: Effect of different casting techniques on cast Al 7075

Al 7075 is produced using various casting processes like gravity die casting, green sand moulding, and investment casting. The described processes differ by their mould characteristics and their ultimate effect on the microstructure and mechanical properties. The difference in the heat dissipation of the moulds creates an effective thermal gradient, which causes a change in the microstructure and mechanical properties. The key aspect of different casting techniques is their mold characteristics. The molds are mainly differed by thermal conductivity (W/m.K), and thermal diffusivity (m<sup>2</sup>/s). Pehlke <sup>[312]</sup> studied the computer simulation of sand mold casting and considered a parameter of thermal conductivity and thermal diffusivity of the mold. Hock <sup>[313]</sup> also studied sand mold characteristics for aluminium casting and predicted casting defects like gas porosity, inter-dendritic porosity, surface porosity, and centerline shrinkage, which is difficult to study by conventional solidification. Xu et al. <sup>[314]</sup> collected data for the investment casting shell to determine

thermal properties data by simulation and experimentation. However, it is another aspect of the study. In general, the thermal diffusivity of the sand mold, metal mold, and ceramic mold. The purpose of the study here is to understand the segregation morphology of the 7XXX aluminium alloy by applying different casting techniques. As in this study, in general, the thermal diffusivity ( $\alpha = k/\rho.C_p$ ), (where  $k$  is thermal conductivity,  $\rho$  is density, and  $C_p$  is specific heat) of the sand casting mold is lower than permanent mold casting ( $\alpha_{\text{sand}} < \alpha_{\text{metal die}}$ ), and it is even less than or equal to sand casting in the case of invest casting mold, depending upon the coating thickness of the mold with investment casting. Hence, the solidification starts from the mold wall to the S/L interface and experiences differences in heat dissipation resulting in different microstructural morphology. Not delving into simulation in any great depth, this study is to examine microstructure and mechanical properties.

**4.5.1 Microscopy of Phase IV**

The microstructural of different casting techniques is shown in Figure 4.32 (a) to (c), and the same microstructure is put for natural ageing for 2 years, as shown in Figure 4.32 (e) to (f).

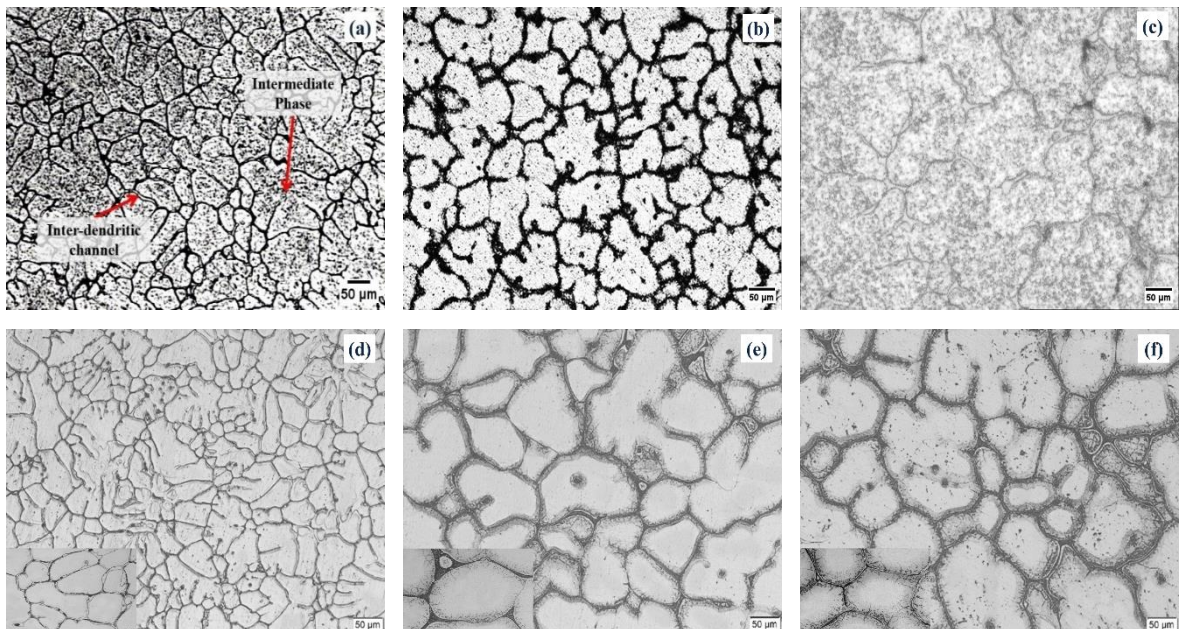


**Figure 4.32 Optical micrographs of different casting techniques of cast Al 7075; a) gravity die casting, b) sand casting, and c) investment casting; natural ageing for 2 years (d-f), respectively.**

Figure 4.32 (a) shows the microstructure of die-cast Al 7075, it depicts segregation of solute

within the grain and in the inter-dendritic channel. Compared to sand casting and investment casting, the grain size differs due to the heat dissipation difference of the processes at mold wall. The microstructure of sand casting is depicted in Figure 4.32 (b), with solutes segregated at the grain boundary but with less segregation within the grain. The grains have a globular shape, which is beneficial for their elongation properties, but because of porosity issues, it has been greatly reduced. In Figure 4.32 (c) the investment casting of Al 7075 is illustrated, which reveals the dispersed segregation of solute within the matrix. It's not a polygon, but the grains appear to be coarse and globular.

After the natural ageing, the segregation changes are observed in all the micrographs. Most segregation shifted at grain boundaries, as shown in Figure 4.32 (d-f). In sand casting, Figure 4.32 (e), the segregation is more at the triple point of the grain boundary, and at the inter-dendritic channel, and this is also observed in investment casting, as shown in Figure 4.32 (f).

As Figure 4.33 illustrates, SEM and elemental mapping of grain and grain boundary shows  $\alpha(\text{Al})$  grain and that solutes are segregated at the grain boundary and are more intense at the triple point. The lamellar eutectic phase at the grain boundary, constitutes  $\eta(\text{MgZn}_2)$ ,  $\text{S}(\text{Al}_2\text{CuMg})$  phases. Figure 4.34 shows the eutectic phase that has been separated at the triple point of the copper-rich grain, and very few eutectics at the adjacent boundaries. The even distribution of Zn and Mg, constituting  $\eta(\text{MgZn}_2)$ , but at the triple junction Cu may form  $(\text{Al}_2\text{Cu})-\theta$  phase. Salarvand et al. <sup>[315]</sup> studied AA5182 high zinc wrought alloy cast by ablation green sand mold casting process and investigated the different cooling effects on the microstructure and mechanical properties. The microstructure and mechanical properties follow the same pattern.

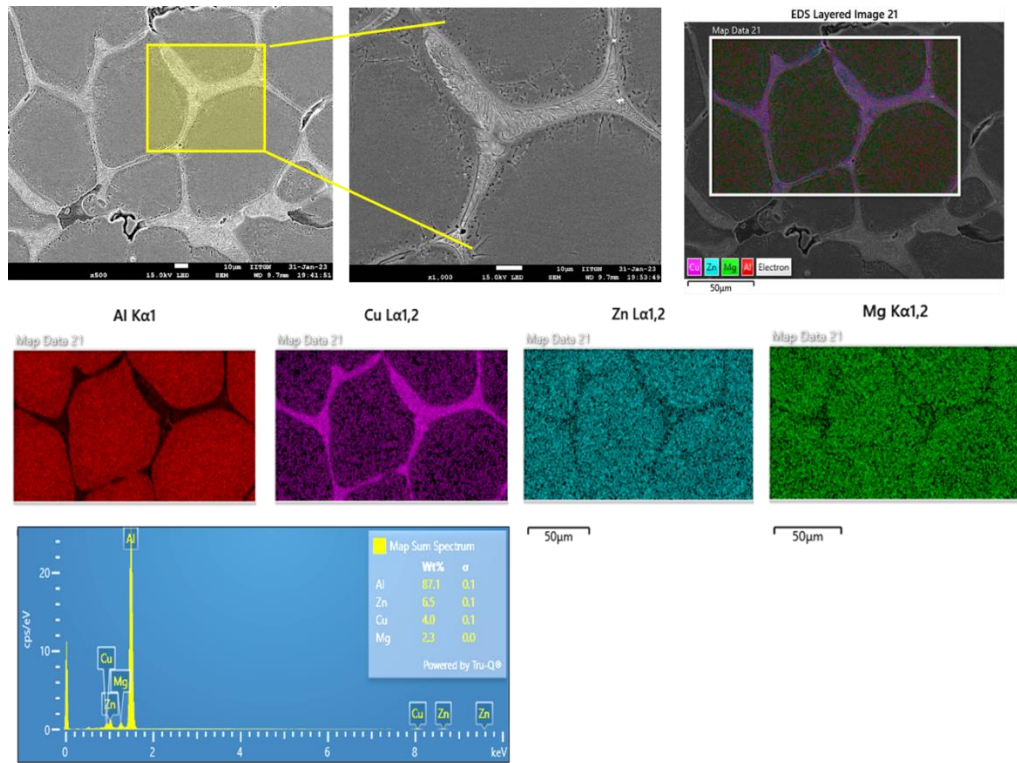


Figure 4.33 SEM and Elemental mapping of as-cast Al 7075 by sand casting technique.

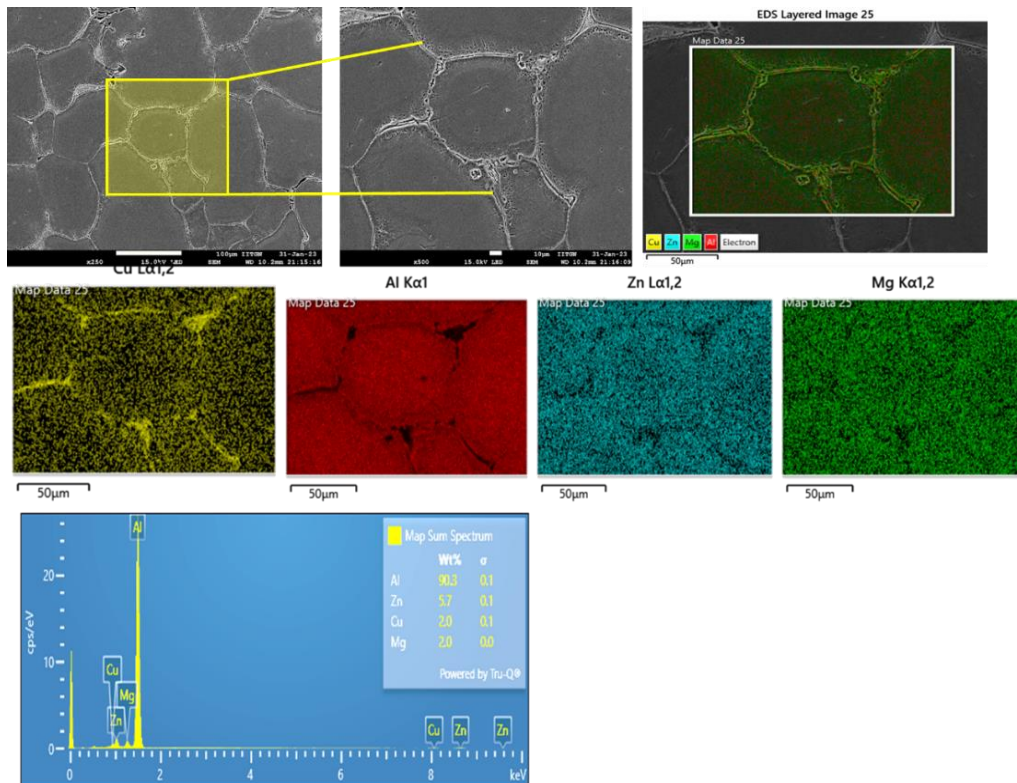


Figure 4.34 SEM and Elemental mapping of as-cast Al 7075 by investment casting technique.

**4.5.2 Mechanical Properties for Phase IV**

Table 4.15 shows the mechanical properties of as-cast Al 7075 produced by different casting techniques.

**Table 4.15 Mechanical properties of cast Al 7075 by different casting techniques.**

Mech. Properties	Casting techniques		
	As-cast	Sand Casting	Investment Casting
Hardness (BHN)	59	100	86
Hardness (BHN) (Naturally Aged)	89 (↑50.84%)	145 (↑45.00%)	140 (↑62.79%)
Micro-hardness (HV <sub>0.5</sub> )	78	105	90
Micro-hardness (HV <sub>0.5</sub> ) (Naturally Aged)	82 (↑5.12%)	161 (↑53.33%)	153 (↑70%)
Tensile Strength (MPa)	183	98	118
Elongation (%)	10	1.5	1.5

Sand and investment casting show the best mechanical properties data for hardness compared to die-cast Al 7075. However, the tensile strength values are lower because of grain boundary precipitation and casting defects.

**4.6 Phase V: Development of cast Al 7075 by alloy addition**

Zinc is the primary alloying element of 7075 aluminium alloy. The addition of 5.1–6.1% zinc makes heat treatable and high strength by precipitation hardening. Also, magnesium in the alloy ranges between 2.1–2.9% helps to produce the MgZn<sub>2</sub> phase. This principal strengthening precipitate is formed when the Zn to Mg ratio exceeds 2 weight percentages. Besides these two, Cu is added (1.2–2%) to improve the precipitation behaviour by forming the GP II zone and η' precipitate, which provides an early ageing stage. The chromium (0.18–0.28%) is added to inhibit the recrystallization, which controls the grain structure.

The high-strength 7XXX aluminium alloys are widely used in aerospace, and automobile industries and their demand increases day by day [167, 201, 316]. Hence, the development of cost-effective Al 7075 from the scrap is in today's demand in this era, as the high use of aluminium alloys in the aerospace and automobile industries increases its inventory in the market.

The addition of alloying elements in pure aluminium has cost-effectively developed the 7075 aluminium alloy. Pure aluminium was as electrical scrap, which is 99.97 % pure. The raw materials and their forms are depicted in Figure 4.35.

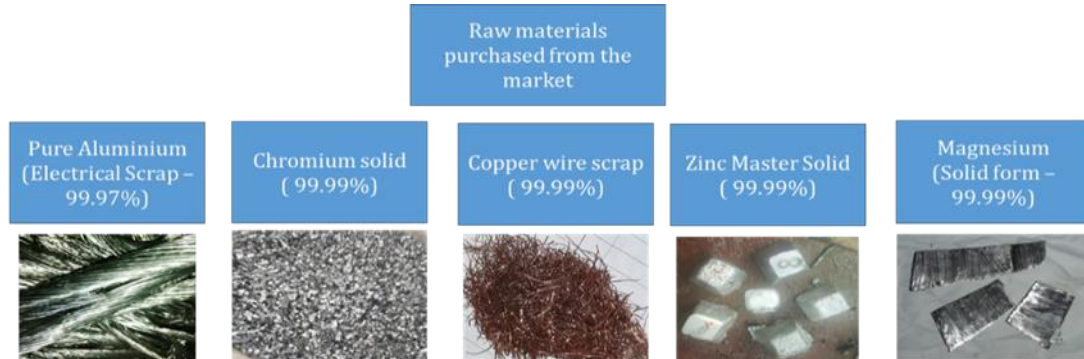


Figure 4.35 Raw materials and their form used to develop Al 7075.

The sequence of addition of the alloying element in pure aluminium melt is important to get the accurate composition of cast Al 7075. The mass balance of the addition of elements is done using simple step calculations. Through binary phase diagrams and oxidation behaviour, we can predict the addition sequence and temperature. Literature states that magnesium is added last as it is oxidized and its recovery cannot reach the limit.

The trials made to achieve the chemical composition within the limit of Al 7075 are given in Table 4.16.

Table 4.16 Mass spectroscopy of trials taken to get chemical composition within a limit of Al 7075.

Elements	Standard composition (wt.%)	1 <sup>st</sup> heat	2 <sup>nd</sup> Heat	3 <sup>rd</sup> Heat	4 <sup>th</sup> Heat
		Trial heats			
Aluminium	87.1–91.4	91.17	89.63	90.11	89.58
Copper	1.2–2	0.161	1.50	1.66	1.75
Magnesium	2.1–2.9	3.00	2.66	2.11	2.389
Zinc	5.1–6.1	5.17	5.442	5.440	5.123
Chromium	0.18–0.28	0.006	0.153	0.118	0.210

The microstructural study of the developed Al 7075 is compared with as-cast Al 7075 wrought Al 7075–T6, and wrought Al 7075–T6, as shown in Figure 4.36 (a) to (c).

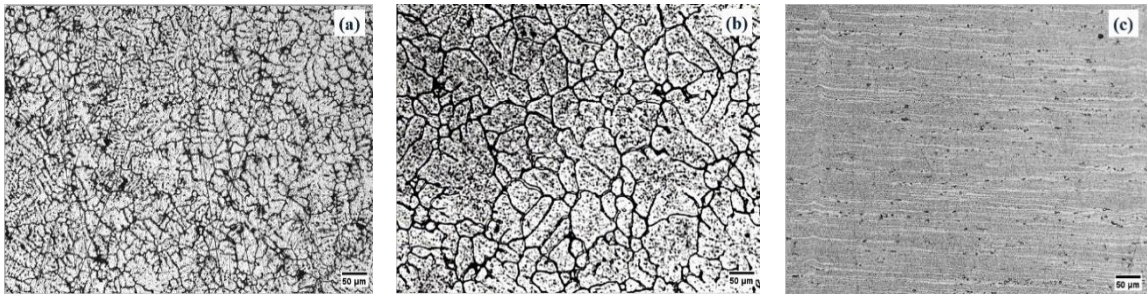


Figure 4.36 Optical micrographs of Al 7075; a) developed cast 7075, b) cast 7075 from wrought, and c) wrought 7075.

As shown in Figure 4.36 (a), the fine columnar dendritic structure is revealed, while coarse columnar grains are formed in as-cast Al 7075 from wrought, as shown in Figure 4.36 (b). Figure 4.36 (c) shows the band structure of elongated grains with fine distribution of precipitates.

The elemental mapping of the developed Al 7075 is shown in Figure 4.37.

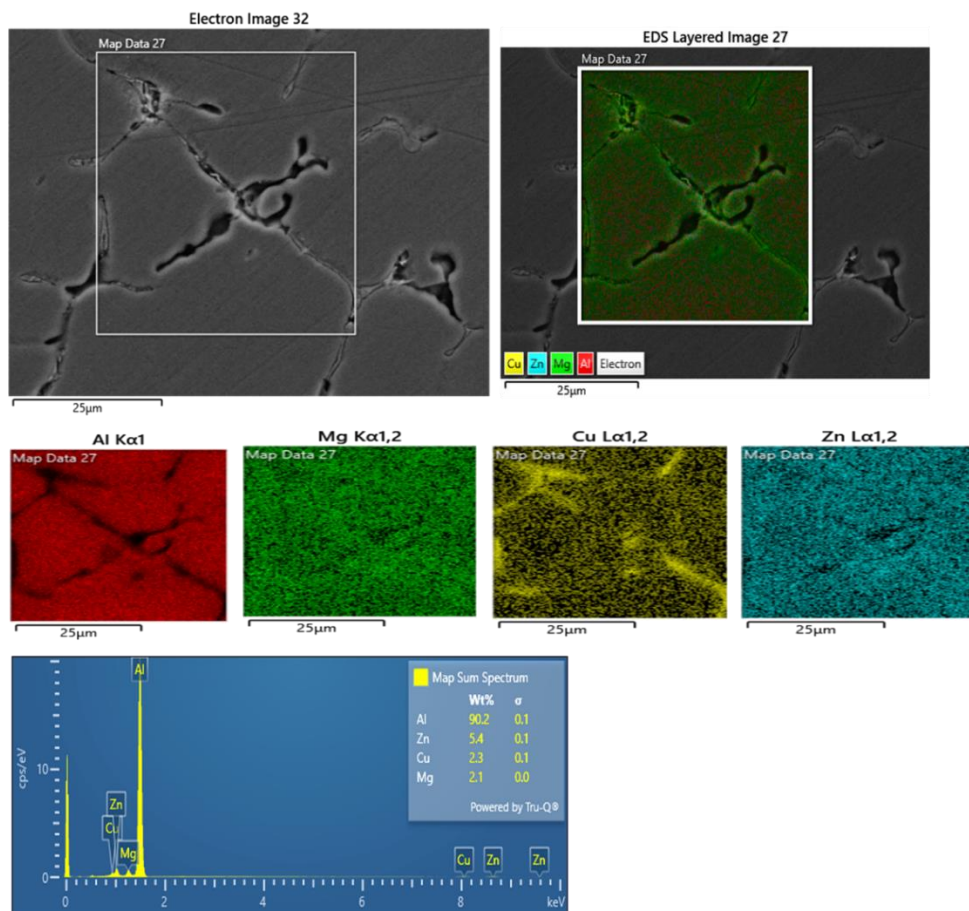


Figure 4.37 Elemental mapping of developed Al 7075.

The elemental mapping of developed Al 7075 shows solute segregated at the triple junction, and it is richer in copper. They are more likely to form either  $\theta(\text{Al}_2\text{Cu})$  or  $\eta'(\text{MgZn}_2)$ .

**Table 4.17 Comparative Mechanical properties of developed cast Al 7075 with Al 7075 cast from wrought and wrought Al 7075.**

<b>Mech. Properties</b>	<b>Developed 7075</b>	<b>Cast from Wrought</b>	<b>Wrought 7075</b>
<b>Hardness (BHN)</b>	94	59	102
<b>Micro-hardness (HV<sub>0.5</sub>)</b>	146	78	112
<b>Tensile Strength (MPa)</b>	212	183	322
<b>Elongation (%)</b>	3%	10%	18%

Table 4.17 shows the comparative mechanical properties of the developed Al 7075. The developed Al 7075 has considerable hardness and tensile strength values compared to wrought, but it is achieved higher than cast from wrought.